ROYAL AERONAUTICAL SOCIETY

RESEARCH ARTICLE

Numerical investigation of air injection in the endwall region of a highly loaded compressor tandem stator configuration

G. Gutiérrez Lupinta[®], S. Giannini[®] and V. Gümmer

Institute of Turbomachinery and Flight Propulsion, Technical University of Munich, Munich, Germany

Corresponding author: G. Gutiérrez Lupinta; Email: gladys.gutierrez@tum.de

Received: 20 October 2024; Revised: 23 September 2025; Accepted: 23 September 2025

Keywords: active flow control; injection slots; tandem vanes; axial compressor; CFD; aerodynamics

Abstract

Flow separation in highly loaded axial compressors remains a major barrier to performance, motivating the search for active flow control strategies. This study investigates air injection to energise low-momentum endwall flow in a tandem stator configuration, representing the first investigation of its kind for tandem vanes. A numerical investigation was conducted, starting with a smooth-casing reference case and progressing to parametric studies of slot geometry (inclination α , jet angle β , radius of curvature R_c , circumferential width w_c), relative injection mass flow rate $\dot{m}_{inj}/\dot{m}_{stall}$ and axial location ζ . The results show how each parameter influences efficiency and pressure ratio, yielding design guidelines: shallow α , moderate β towards the separation zone, relatively large R_c and a balanced $w_c-\dot{m}_{inj}/\dot{m}_{stall}$ combination, best captured through the momentum coefficient C_u and velocity ratio u_{inj}/u_{∞} . Injection near $\zeta \approx 1.2$ (just upstream of separation) proved most effective, and off-design simulations showed larger efficiency gains towards de-throttled conditions, although stall margin was unaffected. Robustness was confirmed through turbulence-model comparisons and injector turbulence variations, which consistently reproduced suppression of suction-side separation. An integrated analysis of aerodynamic losses further showed that injection strategies remain beneficial when loss penalties are considered. The study thus establishes transferable guidelines for injector design in tandem stators, providing a foundation for future optimisation and experimental validation.

Nomenclature

GCI Grid Convergence Index GGI General Grid Interface SC smooth casing

TS tandem stator
DP design point
FV front vane
RV rear vane

Ref refined configurations

Greek symbols

	. 1	1
α	inclination	angie

 β jet angle

 γ ratio of specific heats, air: $\gamma = 1.4$

 Δ increment

ζ injector normalised chordwise location: $0 \le ζ \le 1$ for FV, $1 \le ζ \le 2$ for RV

 η polytropic efficiency

[©] The Author(s), 2025. Published by Cambridge University Press on behalf of Royal Aeronautical Society. This is an Open Access article, distributed under the terms of the Creative Commons Attribution licence (https://creativecommons.org/licenses/by/4.0/), which permits unrestricted re-use, distribution and reproduction, provided the original article is properly cited.

2 Gutiérrez Lupinta et al.

θ	flow angle relative to the axial direction
$\Delta \theta$	flow turning, change in flow angle
П	managama antio

 Π pressure ratio ϕ flow coefficient

 φ generic performance variable used in definition of percentage variation Δ

 ψ work coefficient

 ω pressure loss coefficient

 ω_t mass-weighted total pressure loss coefficient including injection

Latin symbols

 c_{eq} equivalent tandem stator chord length

 C_p static pressure rise coefficient C_f skin–friction coefficient C_u momentum coefficient CoV coefficient of variation DF diffusion factor H normalised span Ma Mach number

m mass flow rate
 p pressure
 T temperature
 N rotational speed
 R_c radius of curvature

s normalised chordwise location, from leading edge (s = 0) to trailing edge (s = 1)

 s_{casing} local circumferential spacing at the casing radius

 t_{mean} average blade thickness u absolute velocity

 u_{∞} freestream velocity at midspan (tandem stator inlet)

w width

 w_a injector width along the local axial direction

 w_c injector width along the local circumferential direction

x radial direction

y circumferential direction

z axial direction

Sub- and superscripts

corr corrected quantity

inj injection inlet

inter interface casing-injector

is isentropic mean mean value out outlet

stall stall condition

s static total

tt total-to-total

 \bar{x} mass–flow average of x

1.0 Introduction

To address the evolving demands of environmentally friendly aviation, it is necessary to maximise engine performance while reducing overall weight, length, fuel consumption and pollutant emissions. The compressor, a critical component, often experiences flow separations in its gaspath, especially near the endwall regions of rotor and stator rows. Therefore, efficient optimisation and flow control methods are essential technologies for enhancing compressor performance in future aircraft engines.

Among the various flow control methods explored, air injection stands out as a particularly effective strategy that has undergone extensive research. Depending on the objective, injection has been applied at the compressor endwalls, for example to suppress rotor tip leakage or corner separations, as well as directly on blade surfaces. In the present context, we review endwall-based strategies applied to stator configurations, which have shown clear benefits for mitigating secondary flows and improving compressor performance. A comprehensive study on a transonic stage [1] examined stator shroud injection in detail, linking slot curvature, location and mass flow to performance metrics, and showed that properly tailored shroud slots can raise pressure ratio, efficiency and stall margin compared to smooth-casing designs. Building on this, an optimisation framework for shroud injection [2] identified slot geometries that maximise efficiency while simultaneously extending stall margin, confirming that carefully designed shroud treatments can yield robust aerodynamic benefits. In cascades, discrete endwall holes were used to target corner separation, and the best results were obtained with low injection angles directed close to the suction surface, while larger angles degraded performance due to mixing losses [3]. Extending this concept, pulsed endwall injection was shown to suppress corner separation effectively, reducing both overall and endwall loss coefficients at comparatively low injection mass flow rates by tuning the actuation frequency and amplitude [4]. Together, these works confirm that endwallbased stator injection is effective for corner flow control, and that injector geometry, actuation mode and orientation strongly influence the achievable aerodynamic benefit.

Beyond endwall-focused concepts, a range of studies has investigated flow control directly on the blade surfaces. Early experiments in the NASA low speed axial compressor applied suction-side slot injection in steady and impulsive modes, achieving notable reductions in stator losses with modest mass flow rates [5, 6]. Subsequent work in the same facility introduced synthetic jets, where oscillatory zero-net-mass-flux blowing further reduced suction-side separation [7]. More recently, blade-end and whole-span slot designs were tested in high-camber stator cascades, with near-streamwise slot orientation chosen to minimise mixing while suppressing both midspan and corner separation [8]. While these approaches confirm the aerodynamic potential of blade-surface actuation, they also require modifications to vane geometry or the integration of actuators within the aerofoil, which introduces considerations of structural integrity and manufacturability.

Meanwhile, tandem aerofoils, employed for their ability to enable higher aerodynamic loading and reduce axial length, exhibit considerable potential for enhancing compressor performance by supporting rotor designs with increased work coefficients and achieving higher pressure rise than traditional single-aerofoil configurations [9–11]. However, the integration of tandem stators poses challenges at the endwalls, where complex flow phenomena can undermine these benefits [12]. To mitigate such effects, several flow control techniques have been applied to tandem stator vanes: near-endwall modifications reduced corner separation by eliminating low-momentum gap flow [13]; endwall boundary-layer suction enabled higher loading without triggering large-scale separation [14]; and non-axisymmetric endwall contouring improved efficiency, particularly at near stall conditions [15]. Despite these efforts, the use of air injection in tandem aerofoil systems remains largely unexplored.

Building on these insights, the present study numerically investigates air injection in the endwall region of a tandem stator, aiming to unlock the full potential of tandem vanes in a highly loaded axial compressor. The work is carried out in two steps: first, identifying the main loss sources in the reference compressor stage; second, designing slot geometries and assessing the impact of injection sites on stage performance. Given the existence of a shrouded cavity at the hub, which limits potential implementation,

Table 1. Design operating point parameters for the low-speed	1.5-stage compressor
--	----------------------

Parameter	Value	Units
Number of blades (IGV/rotor/FV/RV)	40/40/40/40	_
Solidity at mid span (IGV/rotor/FV/RV)	1.00/1.49/1.10/0.87	_
Design rotational speed	1,484.85	RPM
Design mass flow rate	17.922	kg/s
Hub-to-tip ratio	0.8	_
Relative rotor tip gap, $h_{\rm tip}/h_{\rm channel}$	1.75	%
Relative stator sealing clearance, $h_{\text{clear}}/h_{\text{channel}}$	1.00	$ \sqrt[n]{c} $
Design flow coefficient	0.57	_
Design work coefficient	0.58	_
Relative Mach number at rotor tip	0.24	_
Design Π_t	1.03758	_
Design η_{tt}	88.67	%

For the present inlet totals ($T_{t,in} = 288.0 \text{ K}$, $p_{t,in} = 101.142 \text{ kPa}$) and ISA reference conditions ($T_{ref} = 288.15 \text{ K}$, $p_{ref} = 101.325 \text{ kPa}$), $N_{corr} \approx 1,485.24 \text{ RPM}$ and $\dot{m}_{corr} \approx 17.98 \text{ kg/s}$. The listed efficiency and total pressure ratio are evaluated between stations 1 and 2 (see Fig. 3).

and our decision to preserve blade structural integrity by avoiding modifications to the vane geometry, this study focuses on endwall injection at the casing.

2.0 Compressor reference case

For the current study, a 3.5-stage low-speed research compressor was adopted as the reference geometry [16]. This research compressor, situated at the Institute of Turbomachinery and Flight Propulsion of the Technical University of Munich (TUM), is designated for future experimental investigations. The numerical study focuses on the front 1.5-stage, which comprises an inlet guide vane (IGV), a rotor, and a tandem stator. The tandem stator consists of front vanes (FV) and rear vanes (RV) featuring a shrouded cavity arrangement. Table 1 summarises key parameters at the design operating point for the 1.5-stage setup. The decisive non-dimensional design coefficients (flow coefficient $\phi = 0.57$, work coefficient $\psi = 0.58$) indicate a highly loaded configuration, consistent with the Smith-diagram classification of the FRANCC stage [17]. Given the low-speed nature of the research compressor, the total pressure ratio naturally appears low; however, the geometrical relations and non-dimensional parameters are representative of rear high-pressure compressor stages in aero-engines. It should be noted that no experimental data were available for this preliminary configuration at the time of the study; experimental validation was only performed later on the final updated FRANCC geometry.

The reported design-point efficiency and total pressure ratio correspond to the rotor–stator stage of the 1.5-stage domain, evaluated between station 1 (upstream of the rotor) and station 2 (downstream of the stator), as defined in Fig. 3. The values confirm that the FRANCC stage combines high aerodynamic loading with efficiency comparable to conventional designs. Moreover, the FRANCC stage efficiency remains above the values estimated from Smith chart correlations for such a high loading level [18].

The tandem stator configuration was introduced specifically to enable the high aerodynamic loading summarised above. As established in studies of highly loaded compressors [18], increasing the loading coefficient inevitably amplifies secondary and endwall losses and promotes three-dimensional separation within the stator passages. Accordingly, the FRANCC design provides a representative test case in which the tandem stator achieves higher aerodynamic loading than conventional blading but also incurs additional loss mechanisms. This combination of high loading and additional losses motivates the investigation of flow control measures such as air injection aiming to mitigate these effects.

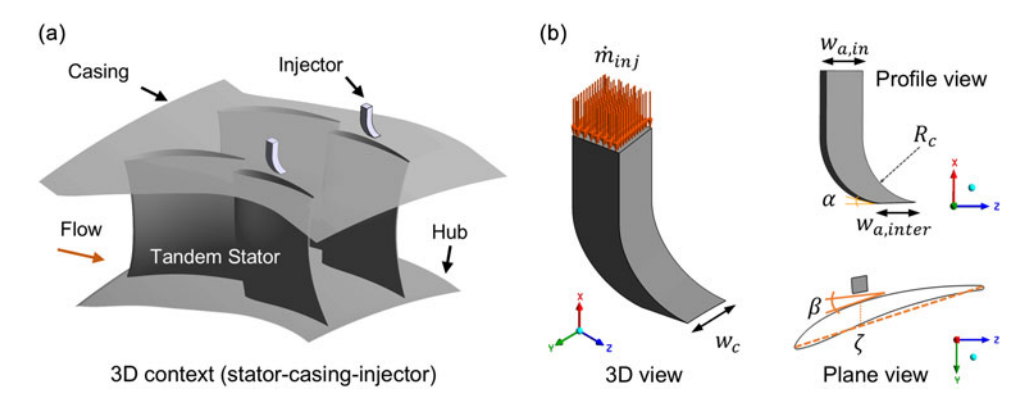


Figure 1. (a) 3D context showing injector location within the compressor. (b) Standard injector geometry and main parameters. The profile view reflects the injector's spatial orientation, while the plane view shows the injector–casing interface and its alignment relative to the blade, highlighting the jet angle β .

3.0 Injection slot parameters

The design of the selected injection slot geometry is based on the Coandă effect [19]. The Coandă effect is the tendency of fluid streams to follow curved surfaces due to viscosity and the pressure drop as the fluid accelerates along curved surfaces, with a pressure gradient-induced centripetal force that ensures sustained adherence. This type of injector is recognised for its non-intrusive application in multistage compressors, capable of generating a wall jet with significant axial velocity along the compressor casing, as documented by Strazisar et al. [20]. The slots are strategically positioned within the stator row on the casing and are uniformly distributed pitchwise, numbering a total of 40 to ensure even flow distribution. Figure 1 shows the injector location within the compressor and its main geometrical parameters, including the profile view, which reflects the spatial orientation of the injector, and the plane view, which shows the injector–casing interface and its alignment relative to the blade.

The key parameters for the injection slots include: the circumferential width w_c and the axial width w_a , defined along the local injector axes approximately aligned with the compressor circumferential and axial directions, with w_a evaluated at the injector inlet $(w_{a,in})$ and at the slot–casing interface $(w_{a,inter})$, the radius of curvature R_c , the injection mass flow rate \dot{m}_{inj} , the slot inclination angle α measured near the injector outlet, the jet angle β and the injector normalised chordwise location ζ . In the injector profile, R_c defines the two circular arcs that connect the vertical inlet with the inclined outlet direction set by α . Both arcs always share the same radius, while their centres shift when α or R_c is varied to remain tangent to the inlet and outlet surfaces. As shown in Fig. 1, the jet angle β is defined as the angle between the injector outlet and the local tangent to the blade surface at the injection point. This angle is crucial for understanding how the injected fluid is oriented relative to the blade. A β of 0° indicates a parallel orientation of the injection direction with the blade at the injection location. Meanwhile, positive β values direct the injection towards the blade, and negative values direct it away from the blade. The dimensionless parameter ζ represents the injector location along the blade chord, normalised from 0 at the leading edge to 1 at the trailing edge for the front vane, and from 1 to 2 for the rear vane. Thus, for the front and rear vanes:

 $\zeta = Z$ (For the front vane)

 $\zeta = 1 + Z$ (For the rear vane)

with Z being the respective chord fraction at the injection location.

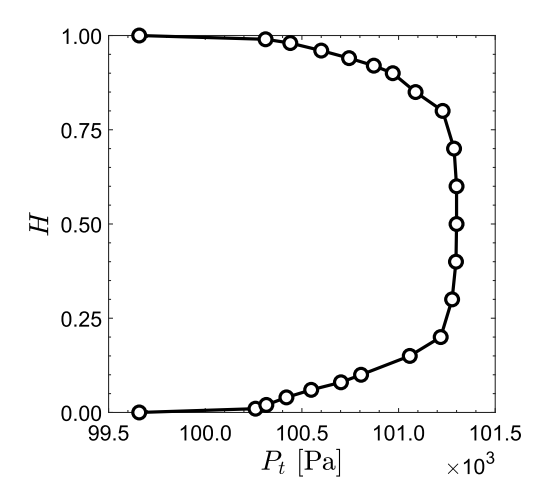


Figure 2. Radial distribution of total pressure prescribed at the inlet.

4.0 Simulation setup

For the numerical study, only one pitch along the 1.5-stage configuration is considered, and all numerical simulations were performed under a steady-state regime using Ansys CFX 2021 R1 as the fluid solver.

In the simulation, boundary conditions were defined with a predetermined radial distribution of total pressure and flow direction characterised by a turbulence fractional intensity of 0.05. The inlet total pressure distribution included a deficit in the upper and lower 20% of the span, based on measured profiles from the Dresden low-speed research compressor [21], whose datum blading was designed to represent a middle high-pressure compressor stage [22]. This choice is consistent with FRANCC numerical setups [17] and with the nature of rear-stage flow fields reported in the literature [23]. The imposed radial distribution is shown in Fig. 2. Additionally, the inlet total temperature was established at 288 K.

For the outlet boundary conditions, the mass flow rate was imposed, adjusting this value for the different operating conditions. This choice provides numerical stability and ensures comparability across cases. Two approaches were applied, differing only in how the outlet value was determined. For the baseline injection case and all subsequent parametric and location studies, the outlet mass flow rate was fixed to match the smooth-casing case at the same operating point, ensuring that the mass flow through the stator domain remained identical. For the smooth-casing speedline, the outlet mass flow rate was directly varied, while for the injection speedlines the outlet value was adjusted so that the resulting inlet mass flow matched the smooth-casing case at each operating point, enabling direct comparison of overall compressor performance. The fluid was modeled as an air ideal gas, while the turbulence model used was the shear stress transport (SST) model. This choice is consistent with the original FRANCC design simulations of Hopfinger [24], where SST was applied with fully turbulent boundary layers and 5% inlet turbulence, and with subsequent tandem-stator investigations by Straccia and Gümmer [15]. The SST model has also shown good performance in predicting separated flows [25], and was successfully validated against detailed experimental data in a similar low-speed tandem-stator compressor (Dresden LSRC) [11].

To ensure effective solver control, a high-resolution model was adopted for both the advection scheme and turbulence. The interfaces between rotor–IGV and rotor–tandem stator were modeled using a mixing plane. Within the shrouded tandem stator region, the cavity–stator and cavity–cavity interfaces contained small non-overlapping portions due to mesh topology and periodicity constraints. To handle such cases, the replicated general grid interface (GGI) option was applied in computation fluid dynamics (CFX), which in practice is activated via the frozen rotor setting with specified pitch angles. This ensured

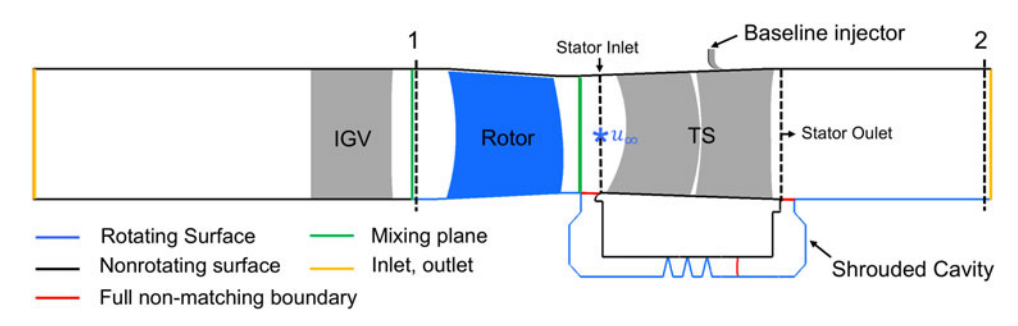


Figure 3. Meridional view of the reference low-speed 1.5-stage axial compressor, showing the injector baseline geometry and performance measurement locations.

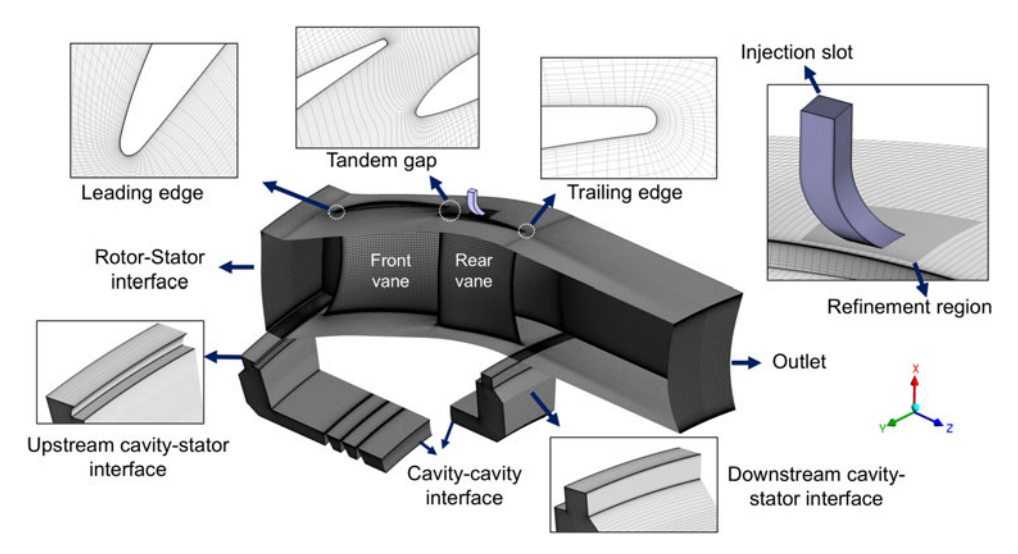


Figure 4. Overview of the mesh for the tandem stator with an injector slot, highlighting the casing refinement and the cavity mesh with its interfaces to the main flow path.

stable and consistent interpolation across the non-overlapping, non-conformal interface regions in the present setup. The meridional view of the 1.5-stage setup is presented in Fig. 3, with some details of the interfaces, boundary conditions and station planes used for evaluating stage performance.

On the other hand, the injection slot within the stator casing was designed with CATIA V5. For its inlet boundary conditions, the injection mass flow rate and total temperature were specified. The casing and the injection slot were connected through a non-conformal interface using a GGI, which facilitates connections of non-matching meshes, allowing for differences in node locations, element types and surface extents [26]. To ensure accurate resolution of the slot–casing interaction, the mesh resolution of the casing surface in the vicinity of the injector interface was locally refined (see also Fig. 4). The casing and injector walls were modelled as smooth, no-slip, adiabatic boundaries. Convergence was considered attained when the coefficient of variation (CoV), defined as the ratio of standard deviation to the mean value, of polytropic stage efficiency, total pressure ratio and inlet mass flow rate all reached magnitudes on the order of 1×10^{-5} , assuring the normalised residuals are below 1×10^{-5} and imbalances below 1×10^{-3} .

The mesh for the 1.5-stage compressor was created using AutoGrid5[™] version 17.1 [27]. A structured grid employing a conventional O4H topology and standard quality criteria was applied, setting the

	$\phi = \Pi_{tt} \left[ext{-} ight]$	$\phi = P_t$ [Pa]	$\phi = \dot{m}_{inj} [\text{kg/s}]$
$\overline{N1, N2, N3} (\times 10^6)$	22.78, 9.83, 3.91	22.78, 9.83, 3.91	0.053, 0.46, 1.79
r_{21}	1.323	1.323	1.57
r_{32}	1.36	1.36	2.05
ϕ_1	1.03754	104,915	0.001355
ϕ_2	1.03758	104,916	0.001362
ϕ_3	1.03769	104,919	0.001392
p	3.1	3.39	7.61
ϕ_{ext}^{21}	1.037511	104,914.37	0.0013933
e_a^{21}	0.00386%	0.000953%	2.124%
$\phi_{ext}^{21} = e_a^{21} = e_{ext}^{21}$	0.00279%	0.000602%	0.071%
GCI_{fine}^{21}	0.00349%	0.000752%	0.088%

Table 2. Grid convergence index (GCI) study results

 N_1, N_2, N_3 : cell counts for fine, medium and coarse grids; subscripts 1,2,3 refer to these grids; r_{21}, r_{32} : grid refinement ratios; p: observed order of accuracy; ϕ_1, ϕ_2, ϕ_3 : values of ϕ on grids 1–3; ϕ_{ext}^{21} : Richardson extrapolated value; e_a^{21}, e_{ext}^{21} : approximate and extrapolated relative errors; GCl_{fin}^{21} : fine-grid GCI for grid pair (2,1).

cell size closest to the wall at 3e-6, corresponding to a dimensionless wall distance of $y^+ \approx 1$. Almost the entire wetted surface satisfies this target, with only very few isolated cells (at leading edges, tip gap and cavity) reaching up to maximum $y^+ \approx 3$, which remains within the viscous sublayer and is acceptable for the turbulence models applied. For the slot, ICEM CFD was utilised to develop a structured grid. The final grid resolutions for both the reference compressor and the refinement area where the injector is placed were determined through a mesh independence study according to the grid convergence index (GCI) method of Celik et al. [28], to ensure accurate and mesh-size independent results. The study considered parameters such as the stage total pressure ratio (Π_n) and total pressure (P_t) at the stator outlet for the 1.5-stage setup, along with the mass flow rate (\dot{m}_{inj}) for the injector, as detailed in Table 2.

The final selected mesh comprises approximately 9.83×10^6 cells, divided among 1.46×10^6 for the IGV, IGV, 1.49×10^6 for the rotor, 4.05×10^6 for the tandem stator (TS), and 2.83×10^6 for the shrouded cavity of the compressor. Approximately 0.5×10^6 cells are allocated to the refinement area to ensure sufficient resolution. For a standard injector geometry with a width of 6 mm, the model incorporates at least 0.3×10^6 cells, with this number proportionally increasing for larger widths. Figure 4 provides an overview of the mesh for the tandem stator with one standard injector positioned at the casing. The zoomed-in view details the mesh of the injector and the refinement in the casing region.

5.0 Results and discussion

In this section, we present the outcomes of our analysis, focusing on key performance indicators. It is important to note that unless explicitly stated otherwise, all variables mentioned herein refer to their mass flow-averaged values. Specific instances or locations where non-averaged or instantaneous values are considered will be clearly identified.

5.1 Smooth casing case

This section examines the aerodynamic performance of the compressor in its baseline configuration, termed the smooth casing (SC) case. In Fig. 5, the speedline for the reference stage is presented, showing the mass flow averaged total-to-total polytropic efficiency ($\bar{\eta}_u$) and the mass flow averaged total pressure ratio ($\bar{\Pi}_{tt}$), plotted against the normalised mass flow rate with respect to the design point mass flow rate (\dot{m}/\dot{m}_{DP}), differentiating between stage and rotor.

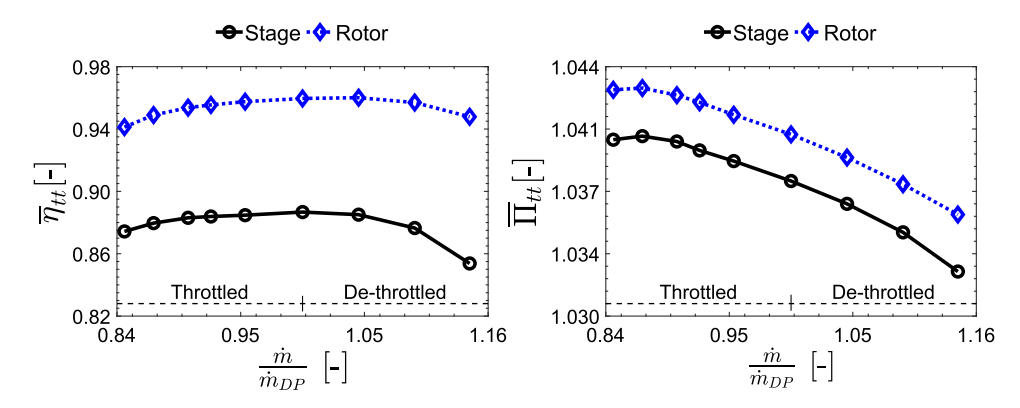


Figure 5. Speedline showing mass flow averaged total-to-total polytropic efficiency $(\bar{\eta}_{tt})$ and total pressure ratio $(\bar{\Pi}_{tt})$ for the compressor stage and rotor.

For a perfect gas with constant γ (air: $\gamma = 1.4$), these quantities are defined as:

$$\eta_{tt} = \frac{\gamma - 1}{\gamma} \frac{\ln (P_{t2}/P_{t1})}{\ln (T_{t2}/T_{t1})},\tag{1}$$

$$\Pi_{tt} = \frac{P_{t2}}{P_{t1}},\tag{2}$$

where P_{t1} and T_{t1} are the mass–averaged total pressure and temperature at inlet of the rotor-stator stage (station 1 in Fig. 3), and P_{t2} and T_{t2} are the corresponding values at the stage outlet downstream of the stator (station 2).

At the design point, the stage achieves a total pressure ratio Π_{tt} of 1.0376, a polytropic efficiency $\bar{\eta}_{tt}$ of 88.67%, and an inlet corrected mass flow \dot{m}_{DP} of 17.922 kg s⁻¹. The numerical speedline indicates that the compressor operational range is constrained, with numerical stall occurring at approximately 85% of \dot{m}_{DP} , corresponding to $\dot{m}_{stall} \approx 15.1$ kg s⁻¹. Here, \dot{m}_{stall} is defined as the minimum mass flow rate at which the simulation remains numerically stable. The rotor performance significantly influences the overall stage behaviour, dominated by a double-leakage tip clearance flow [16]. Accordingly, the current study focuses on stator endwall injection to enhance performance rather than expanding the stall margin.

Figure 6 presents normalised spanwise mass-averaged profiles of key aerodynamic parameters within the stator: the stage polytropic efficiency $\bar{\eta}_u$, the static pressure rise coefficient $\overline{C_p}$ (ratio of static to dynamic pressure rise), the total pressure loss coefficient $\bar{\omega}$ (normalised total pressure loss) and the axial velocity $\overline{u_z}$ at both the leading and trailing edges.

As observed, the total pressure loss coefficient exhibits a pronounced increase towards the casing, correlating with the efficiency drop and indicating significant aerodynamic losses. This increase is consistent with the abrupt rise in $\overline{C_p}$ over 80% span, suggesting a rapid conversion of dynamic pressure into static pressure. The axial velocity profiles at the leading and trailing edge of the stator vanes further reinforce these observations: at midspan, a natural reduction from annulus divergence and density rise is visible. However, the reduction is more pronounced near the casing starting at H=0.7 in the trailing edge profile, contrasting with the less pronounced velocity reduction at the leading edge, beginning at about H=0.85. This pattern suggests a growth in boundary-layer thickness, influenced by the adverse pressure gradient, leading to the deceleration of fluid particles which can precipitate flow separation. Additionally, the blockage from upstream rotor tip leakage contributes to low-momentum flow, further impacting stator performance. Similar phenomena are observed near the hub, associated with the shrouded cavity interaction, although we omit their detailed discussion since the focus is placed on the near-casing endwall region.

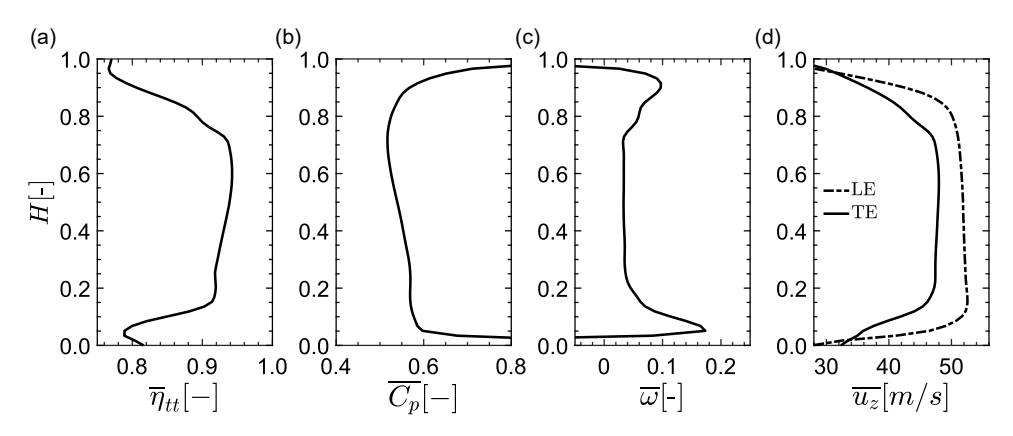


Figure 6. Normalised spanwise profiles at design point: (a) stage efficiency $\bar{\eta}_{tt}$, (b) stator \bar{C}_p , (c) stator $\bar{\omega}$, and (d) axial velocities \bar{u}_z at the leading edge and trailing edge of the stator vanes.

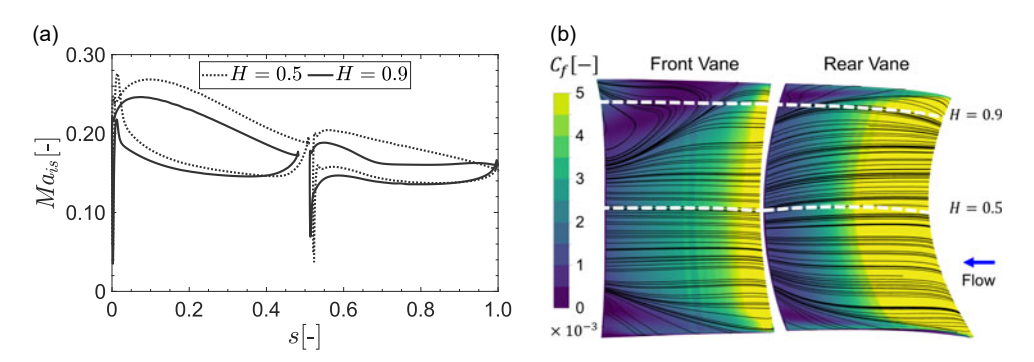


Figure 7. (a) Isentropic Mach number profiles at mid-span (H = 0.5) and near the casing (H = 0.9), plotted against the normalised chordwise location s from the leading edge of the front vane to the trailing edge of the rear vane; (b) Limiting streamlines and friction coefficient C_f contours.

The flow behaviour over the blade surfaces can be examined in Fig. 7. Figure 7(a) shows the blade loading profiles of the isentropic Mach number Ma_{is} at two critical spanwise locations, mid-span H = 0.5 and near the casing H = 0.9. The profiles are plotted against the normalised chordwise location s, which extends from s = 0 at the leading edge of the front vane to s = 1 at the trailing edge of the rear vane. Figure 7(b) presents the corresponding limiting streamlines and the contours of the friction coefficient C_f . A pronounced loading is observed on the front vane compared to the rear vane, suggested by the greater separation between the suction and pressure sides.

This is confirmed by an overall diffusion factor DF of 0.52 considering an equivalent chord length, while the individual values for the front and rear vanes are 0.44 and 0.27, respectively. At H = 0.5, the Ma_{is} profiles exhibit smooth gradients for both blade profiles and consistently higher loading along the chord compared to H = 0.9. This contrast indicates the influence of three-dimensional effects and endwall interactions. At H = 0.9 the rear vane shows a flattening of the Ma_{is} profile around $s \approx 0.7$, which signals a reduced diffusion capacity due to flow detachment. The limiting streamlines confirm the near-casing corner separation, consistent with the local decrease in C_f . Such complex secondary flow phenomena at the endwall region in tandem configurations have previously been attributed to the interaction between the front and rear vanes [29].

These findings imply that the aerodynamic performance can be further improved, potentially through targeted flow control strategies. The subsequent sections will discuss the implementation of endwall

Parameter	Design Space	Baseline	Norm. Range [%]	Norm. Baseline [%]
Already dimension	aless			
ζ [–]	[0.1, 1.7]	1.4	_	_
α[°]	[2.5, 10]	5	_	-
$oldsymbol{eta}$ [$^{\circ}$]	[-15, 45]	0	_	-
$\dot{m}_{inj}/\dot{m}_{stall}$ [%]	[0, 1]	0.5	_	_
Dimensional (with	normalised count	erpart)		
$T_{t,inj}$ [K]	Constant	294	100	100
R_c [mm]	[5, 12.5]	10	3–8	6
w_c [mm]	[6, 12]	6	7–14	7
$W_{a,in}$ [mm]	Constant	6	100	100
$W_{a,inter}$ [mm]	Constant	6	100	100

Table 3. Design space parameters and baseline values; dimensional parameters are expressed with normalised counterparts in %

 R_c normalised by equivalent tandem stator chord $c_{eq} = 0.16$ m; w_c normalised by local spacing at the casing $s_{casing} = 0.086$ m; $w_{a,in}$ and $w_{a,inter}$ normalised by average blade thickness $t_{mean} = 6$ mm; $T_{t,inj}$ normalised by mean total temperature of the 3.5-stage reference compressor $T_{t,mean} = 294$ K

injection as a means to address these identified shortcomings and thereby improve the stator and stage performance.

5.2 Baseline injection case

A baseline injection case to conduct parametric studies on various geometrical variables is considered. The anticipated flow separation zone on the suction side of the RV suggests that locations on the suction side are promising for flow energisation via air injection. Accordingly, the baseline location for air injection has been selected at roughly 40% of the rear vane chord length. Following the definition presented in Section 3, the normalised chordwise location, denoted by ζ , is set to 1.4. Table 3 outlines the preliminary design space parameters and the values selected for the baseline case.

The injection total temperature, $T_{t,inj}$, is set at 294 K, corresponding to the arithmetic mean of the annulus mass-averaged total temperatures at the inlet and outlet of a 3.5-stage reference simulation (288 K and 300 K, respectively). This choice reflects the mean compressor thermal state, consistent with the assumption that the injection source is extracted from later stages [30]. Expressed in normalised form, this corresponds to $T_{t,inj}/T_{t,mean} = 100\%$, where $T_{t,mean} = 294$ K. This avoids unrealistically favourable cooling effects, ensuring the injected air temperature is representative of conditions in the injection region. Additionally, a turbulence intensity of 5% was prescribed at the injector inlet, consistent with the compressor inlet boundary condition.

To ensure minimal disturbance to the main flow, initial values are chosen conservatively. In light of prior research [31], minimising injection angles is critical; hence, the adoption of relatively low α values. The initial injection jet is aligned tangentially with the blade at the injection location ($\beta=0$). To minimise losses in efficiency, it is preferable to keep the injection mass flow rate to a minimum [32]. The injection mass flow rate is normalised with respect to the stall mass flow rate ($\dot{m}_{inj}/\dot{m}_{stall}$), where \dot{m}_{stall} is taken from the smooth-casing simulation. The initial widths of the injector are equivalent to the average blade thickness, being specified as 6 mm.

To improve transferability, dimensional injector parameters are reported together with normalised counterparts. The Coandă radius is scaled by the equivalent tandem stator chord $c_{eq} = 0.16$ m, the circumferential slot width w_c by the local spacing at the casing $s_{casing} = 0.086$ m, and the injection temperature by the mean total temperature of the 3.5-stage compressor $T_{t,mean} = 294$ K. For the present study, the widths defined at the inlet $w_{a,in}$ and at the interface $w_{a,inter}$ remain constant and are normalised by the

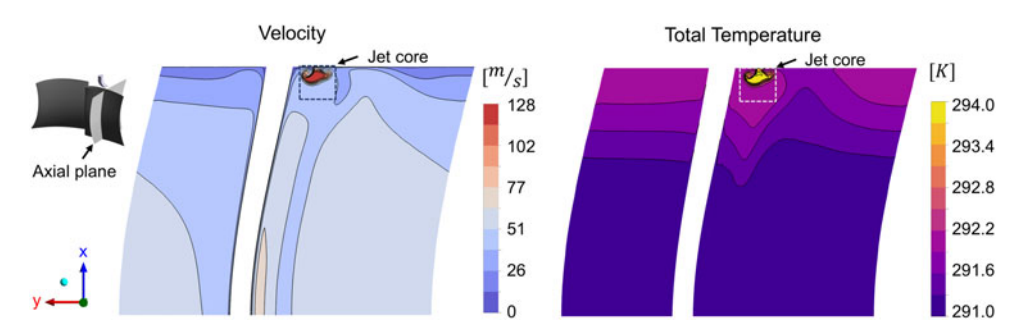


Figure 8. Baseline injection case at design point. Velocity magnitude (left) and total temperature (right) on an axial plane just downstream of the slot exit, cropped to the upper 50% span. The dashed box marks the jet core patch (upper 10% span) used in Table 4.

average blade thickness $t_{mean} = 6$ mm. Expressing these values in percentage form highlights their scale relative to the compressor geometry, while absolute values are retained for clarity.

The boundary condition approach for mass flow control in the baseline case, as well as in the subsequent parametric and location studies, follows the 'equal outlet mass flow' method described in Section 4, i.e. the outlet mass flow rate is imposed and set to match that of the smooth-casing case at the design point. For completeness, the baseline case was also repeated using the alternative 'equal inlet mass flow' strategy from Section 4, which likewise imposes the outlet mass flow rate but determines its value so that the resulting inlet mass flow matches the smooth-casing case. Due to the small injection fraction employed, differences in stage total pressure ratio and efficiency were within $\pm 0.016\%$ and $\pm 0.03\%$, respectively. In the subsequent sections, all reported increments were above these thresholds. Additionally, we selected an exit Mach number for the injector ($Ma \approx 0.35$), which falls within the range of the maximum Ma observed in the compressor, to ensure a realistic operational context. This conservative approach avoids inducing high-speed flow phenomena that could compromise flow stability and aerodynamic integrity.

To provide context for the injection conditions, Fig. 8 presents the local flow field for the baseline injection case at the design point showing velocity and total temperature contours. The contours are shown on an axial plane located immediately downstream of the slot exit, cropped to the upper 50% span for clarity. The *jet core patch*, centred on the high-velocity jet emerging from the slot within the upper 10% span, is indicated in the figure. For comparison, Table 4 reports mass-averaged flow properties for this jet core patch as well as for the whole-pitch average in the same upper-span band, with the smooth-casing whole-pitch average also listed for reference. The high-velocity jet core is clearly distinguishable from the surrounding endwall flow, while the small differences between the smooth-casing and injection whole-pitch averages confirm that the influence is local. In the jet core, total temperature and total pressure are higher than the surrounding flow, while static temperature and pressure are slightly lower, consistent with the higher local Mach number of the injected stream.

5.3 Injector parametric study

Initially, we examine the isolated impacts of key injection parameters such as the inclination angle (α) , jet angle (β) , and radius of curvature (R_c) , keeping the normalised chordwise location (ζ) at 1.4. After establishing optimal values for α , β and R_c , our focus shifts to assess the interaction between the circumferential width (w_c) and the relative injection mass flow rate with respect to the stall mass flow rate $(\dot{m}_{inj}/\dot{m}_{stall})$, given their combined influence on achieving the desired exit injector Mach number within specified limits. This process refines our baseline towards an enhanced configuration. Finally, we explore variations in ζ values to determine effective injector locations.

upper 10% span for the baseline infection and smooth casing					
Region	$u [{\rm m s^{-1}}]$	$T_t[K]$	T_s [K]	P_t [Pa]	P_s [Pa]
Jet core patch (baseline inj.)	67.73	292.63	289.86	106,437	102,895
Whole pitch (baseline inj.)	43.36	291.96	290.87	104,698	103,370
Whole pitch (smooth casing)	38.43	291.85	291.08	104,305	103,345

Table 4. Mass-averaged flow properties in the jet core patch and in the whole pitch of the upper 10% span for the baseline injection and smooth-casing

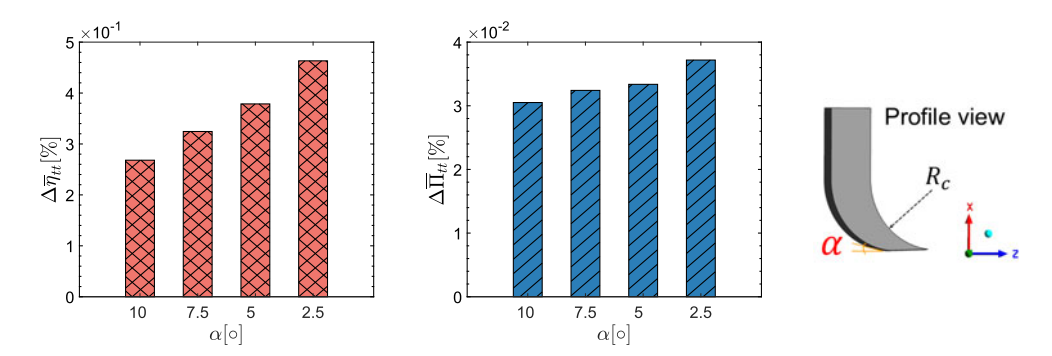


Figure 9. Aerodynamic influence of inclination angle α , schematic inset shows definition of α .

The subsequent figures illustrate the influence of injection parameters on key aerodynamic performance metrics, showing variations Δ for increments in stage variables such as polytropic efficiency η_u and total pressure ratio Π_u , which were defined previously in Equations (1) and (2). The percentage variation Δ for any performance metric, such as η_u or Π_u , is calculated according to Equation (3) as

$$\Delta = \left(\frac{\varphi_{inj}}{\varphi_{SC}} - 1\right) \times 100\%,\tag{3}$$

where φ_{inj} represents the value of the variable for the injection case, and φ_{SC} represents the value for the smooth casing case.

These parameters are evaluated as mass-flow averaged values at the specified stations 1 and 2. The analysis utilises standard definitions, primarily focusing on the aerodynamic impacts without directly accounting for the costs associated with injection. However, the influence of the injected flow is inherently captured in the outlet conditions, affecting the polytropic efficiency and total pressure ratio. This relationship is further explored through the use of the momentum coefficient C_u , which correlates with the aerodynamic performance improvements observed. Section 5.9 provides a detailed discussion of injection losses and introduces the alternative total pressure loss coefficient ω_t , which incorporates the contributions of both the main and injected flows.

5.3.1 Influence of inclination angle

Figure 9 shows how the injector slot inclination angle α affects aerodynamic performance; smaller values of α enhance stage efficiency. The trend confirms that a more tangential introduction of flow reduces disturbance to the main passage and promotes smoother integration of the injected jet, consistent with the findings of Cao et al. [3]. In the present study, the lowest tested angle of $\alpha = 2.5^{\circ}$ yielded the largest efficiency and total pressure ratio increments ($\Delta \eta_u = 0.463\%$, $\Delta \Pi_u = 0.037\%$).

However, from a numerical perspective, angles approaching zero can present challenges in maintaining mesh quality, particularly after the slot curvature, while from a design perspective, very shallow angles may require higher injection pressures to overcome flow resistance. For these reasons, an angle of



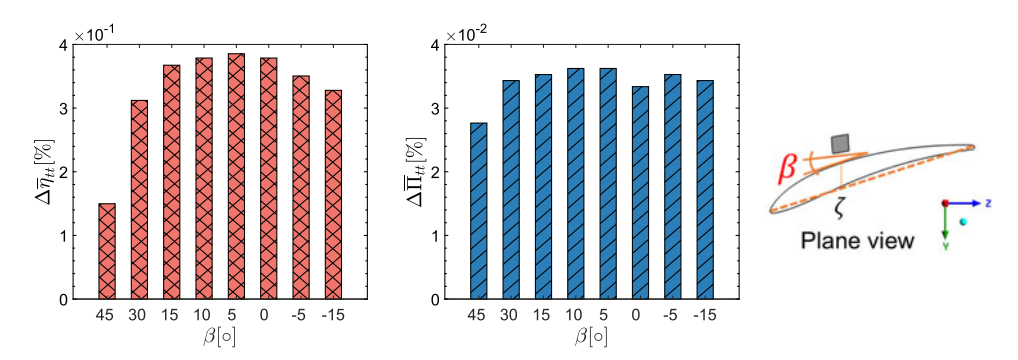


Figure 10. Sensitivity of jet angles to aerodynamic parameters, schematic inset shows definition of β .

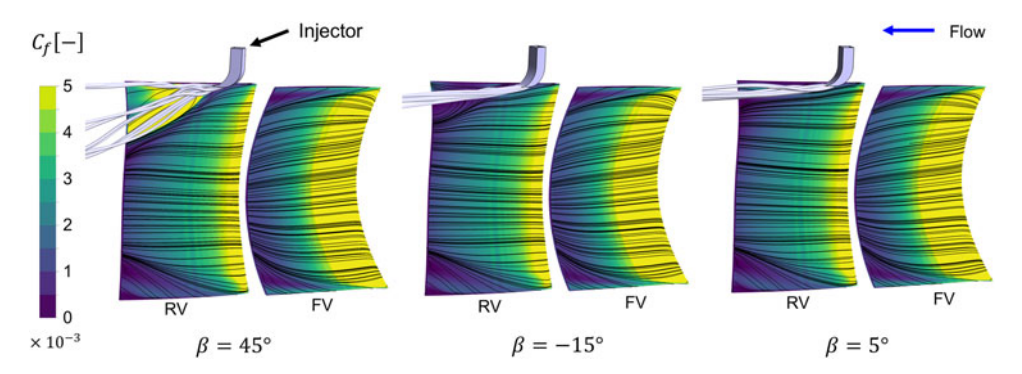


Figure 11. Blade limiting streamlines with surface friction coefficient C_f contours and 3D injector velocity field for different β angles.

5° was adopted in the enhanced configuration as a practical compromise, ensuring sufficient mesh quality and realistic injection requirements while preserving the aerodynamic benefit of a low inclination. Overall, the results suggest that for endwall slot concepts, the inclination angle should be kept relatively small to introduce the flow as tangentially as possible and energise the boundary layer.

5.3.2 Influence of jet angle

The influence of the jet angle β on the performance can be seen in Fig. 10. At the baseline rear-vane suction-side location, maintaining the jet angle β within a moderate range of 0°–20° yields consistent gains in efficiency and total pressure ratio, with a peak increment in η_{tt} of 0.385% at $\beta = 5^{\circ}$. Larger deflections, such as $\beta = 45^{\circ}$, as well as negative angles at this location, proved ineffective in suppressing the corner separation and reduced overall performance. The observed variability confirms that η_{tt} is more sensitive to β (CoV = 0.220) than Π_{tt} (CoV = 0.076). Figure 11 displays 3D injector exit velocity streamlines and blade limiting streamlines with surface friction coefficient C_f contours for $\beta = 45^{\circ}$, 5°, and -15° , clearly showing that jets at extreme or negative angles fail to control the separation zone, whereas a moderate positive orientation redirects momentum effectively into the suction-side corner region. While $= 5^{\circ}$ corresponds to the local peak, these findings emphasise a broader guideline: moderate positive angles directed towards the RV suction side are effective, whereas extremes should be avoided. The key point is to direct smoothly the injected flow towards the separation region in order to energise the endwall flow. Later in the location study it is shown that negative β can become beneficial when the injector is positioned on the FV pressure side, highlighting the dependence of the optimal jet angle on slot location relative to the separation zone.

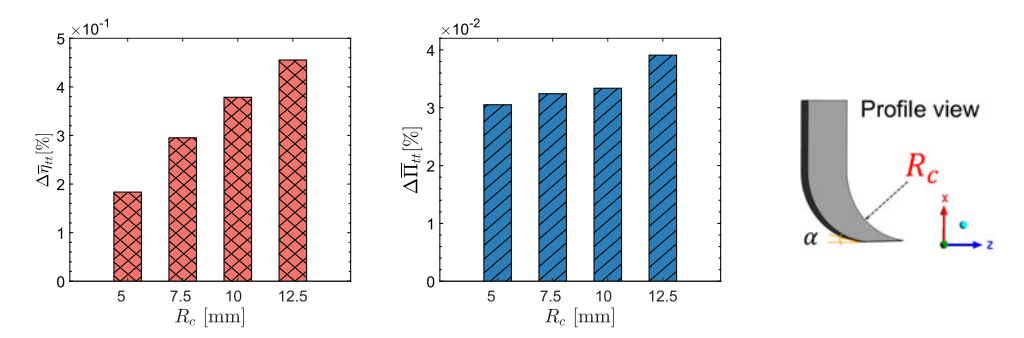


Figure 12. Aerodynamic influence of the injector radius of curvature R_c , schematic inset shows definition of R_c .

5.3.3 Influence of radius of curvature

The impact of the injector radius of curvature (R_c) on injection effectiveness is shown in Fig. 12, where an increase in R_c improves performance, consistent with the findings of Dinh and Kim [1]. In the present study, the largest tested value of $R_c = 12.5$ mm produced the highest increments in η_{tt} (0.455%) and Π_{tt} (0.039%). For a Coandă-type injector, a larger curvature promotes sustained flow attachment on the convex side, enhancing acceleration through the induced radial pressure gradient [33]. This yields a higher-momentum jet that more effectively mitigates separation zones and improves endwall mixing.

As R_c increases, the injector can sustain higher exit velocities, an effect comparable to decreasing the inclination angle α . In this study, values beyond $R_c = 12.5$ mm were not investigated, as they produced exit velocities above the specified limits. Moreover, larger R_c typically requires higher injection pressures to overcome the increased flow resistance. Overall, the results indicate that using a relatively large radius of curvature is beneficial to promote Coandă attachment and jet acceleration, provided the resulting exit velocity remains within realistic limits.

5.3.4 Role of momentum coefficient

The influence on aerodynamic performance of the circumferential width w_c and relative injection mass flow rate $\dot{m}_{inj}/\dot{m}_{stall}$ is analysed in combination due to their strong interrelated effects. From a physical standpoint, an increase in $\dot{m}_{inj}/\dot{m}_{stall}$ with unchanged geometry leads to higher velocity and momentum. Conversely, an increase in w_c at a constant \dot{m}_{inj} reduces it. Thus, establishing an optimal balance between w_c and $\dot{m}_{inj}/\dot{m}_{stall}$ is crucial.

To this end, we introduce the so-called refined configurations, featuring varying circumferential widths w_c to examine the interaction between w_c and $\dot{m}_{inj}/\dot{m}_{stall}$. Accordingly, the inclination angle α is set at 5° to strike a balance between aerodynamic advantages and mesh quality. The optimal jet angle β of 5° was determined based on its standout performance in preliminary analyses. Moreover, the radius of curvature R_c is fixed at 12.5 mm, aligning with the most favourable outcomes. Assumptions for other parameters remain as specified in the baseline scenario. Details of these configurations are presented in Table 5, exploring a spectrum of w_c values to evaluate their effects within the predefined $\dot{m}_{inj}/\dot{m}_{stall}$ ranges, selected with consideration for the injector exit Mach number restrictions.

To characterise each injection case, the momentum coefficient [34], defined as the ratio of the blowing-flow momentum flux to the free-stream momentum flux under the assumption of incompressible flow with equal injection and mainstream densities, is expressed in Equation (4):

$$C_u = \frac{u_{inj}^2 \cdot w_c}{0.5 \cdot u_{\infty}^2 \cdot c_{eq}} \cdot \sin(\beta)$$
(4)

where C_u is the momentum coefficient, u_{inj} is the velocity of the blowing flow, w_c is the width of the blowing slot, u_{∞} is the freestream velocity, c_{eq} is the equivalent chord length of the tandem stator, measured

 Ref $_1$ Ref $_2$ Ref $_3$ Ref $_4$
 w_c [mm]
 6
 8
 10
 12

 $\dot{m}_{inj}/\dot{m}_{stall}$ [%]
 [0.2, 0.45]
 [0.4, 0.6]
 [0.5, 0.75]
 [0.6, 0.9]

Table 5. Parameters for refined injection configurations

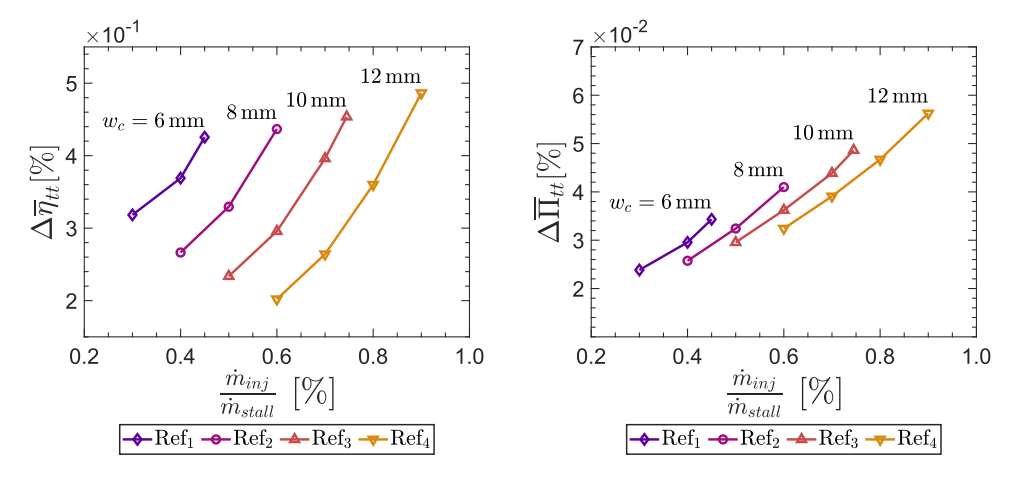


Figure 13. Interplay of w_c and $\dot{m}_{ini}/\dot{m}_{stall}$ on aerodynamic performance.

from the leading edge of the front vane to the trailing edge of the rear vane, and β is the blowing (jet) angle. Here, u_{∞} denotes the mass–flow–averaged freestream axial velocity at midspan of the tandem stator inlet, consistent with the freestream condition used in previous studies [32]; in the present setup $u_{\infty} \approx 60 \text{m s}^{-1}$. This location is annotated in Fig. 3. Since the injector exit Mach number was limited to $Ma \approx 0.35$ (see Section 5.2), density variations are negligible and the simplified form of Equation 4 is valid. Because the jet acts on the near-endwall boundary layer, where the axial velocity is lower than the mid-span freestream, a local normalisation can also be defined. Under equal densities, changing the reference speed to u_{local} rescales the coefficient as $C_u^{(local)} = C_u (u_{\infty}/u_{local})^2$. For the smooth-casing case, the axial velocity at the injector location in the upper 10% of the span is $u_{local} \approx 35 \text{m s}^{-1}$, implying $C_u^{(local)} \approx 2.9 C_u$; this rescaling does not affect the observed trends.

Figure 13 illustrates the effects of the refined configurations on aerodynamic parameters for different injection ratios. At a fixed $\dot{m}_{inj}/\dot{m}_{stall}$, a smaller w_c yields better injection effectiveness, whereas at a constant w_c , a higher $\dot{m}_{inj}/\dot{m}_{stall}$ enhances performance. Judging by the gains in polytropic efficiency and total pressure ratio, Ref₄ emerges as a strong configuration, achieving the highest increments at the peak $\dot{m}_{inj}/\dot{m}_{stall}$ value (0.49% for η_{tt} and 0.056% for Π_{tt}). For similar aerodynamic gains, minimising injection rates can be compensated by decreasing circumferential widths.

The equivalent momentum coefficients C_u are plotted in Fig. 14 against the ratio u_{inj}/u_{∞} , together with a colormap to show the gains in efficiency and total pressure ratio for each case. The analysis reveals findings similar to those of Sarimurat and Dang [34], who proposed an analytical model to predict the effectiveness of steady blowing for boundary layer control, assuming incompressible flow of equal density for both main and blowing streams. The study found that a reduction in the momentum thickness of the boundary layer correlates with the momentum coefficient. Relating the reduction of momentum thickness to an improvement in aerodynamic performance, we observed that at a constant momentum coefficient and blowing angle, the gain is more pronounced with higher blown-to-free stream velocity ratios (lower w_c), as long as the blown flow forward velocity exceeds the free stream velocity. In terms of efficiency, for a constant velocity ratio closer to 1, larger C_u values represented by larger widths are not beneficial. Conversely, for u_{inj}/u_{∞} closer to 2, the improvement correlates proportionally with the

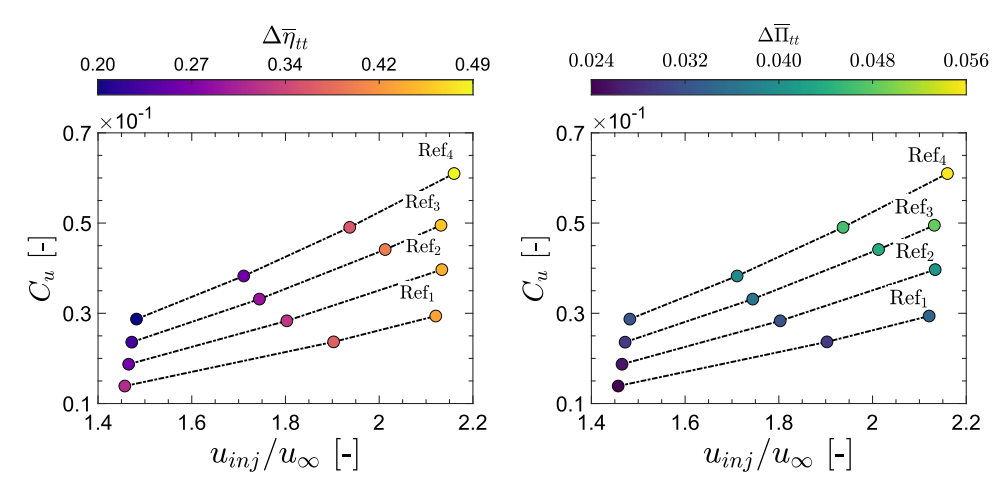


Figure 14. Relationship of C_u and u_{inj}/u_{∞} with aerodynamic performance.

momentum coefficient, as can be seen when comparing the peak cases of every configuration. In terms of the total pressure ratio, higher momentum flow correlates with higher total pressure ratio values for every case of velocity ratio, since we are introducing a higher energy fluid to the main flow.

5.4 Enhanced configuration

To ensure comparability across different study locations, it is critical to maintain a uniform geometry. The role of w_c and $\dot{m}_{inj}/\dot{m}_{stall}$ was already examined through the refined configurations, where their combined influence was assessed through the momentum coefficient and velocity ratios. Those results indicated that smaller w_c values are generally more effective at constant mass flow, but that the benefits can be recovered with higher injection rates. For the subsequent location study, w_c is therefore fixed at 10 mm—consistent with the physical space available in the tandem gap—while $\dot{m}_{inj}/\dot{m}_{stall}$ is set at a representative peak value of 0.75%. This choice (Ref 3) enables consistent comparisons between locations, while still reflecting the trends observed in the broader $w_c - \dot{m}_{inj}$ parameter space. The resulting configuration shows significant enhancements over the smooth-casing case, with increments of 0.43% in η_u and 0.047% in Π_u .

Span profiles, correlating normalised span H with stage and stator aerodynamic parameters for the smooth casing, baseline, and enhanced configurations, are depicted in Fig. 15. The enhanced configuration outperforms in improving stage efficiency and total pressure ratio, especially near the casing, with the injection effect evident downstream of the injection site above H=0.6. Accordingly, the static pressure rise coefficient C_p for both injection cases is above that of the smooth casing case at near casing regions and, to a lesser extent, at mid and lower span zones. Flow redistribution due to injection slightly influences behaviour beyond the casing endwall region. Specifically, for H<0.3, the near-hub region is minimally affected by the endwall injection. Since there is slightly more pressurised flow in this region for the injection cases, the recirculating flow in the shrouded cavity can slightly increase, marginally raising losses [35]. Nevertheless, the overall impact of the injection remains beneficial.

Furthermore, the entropy contours at different axial locations and the axial velocity contour for H = 0.95 are displayed in Fig. 16 for both the smooth casing case and the enhanced configuration. It is evident that the areas of high entropy in the casing corner separation region are considerably reduced, resulting in a smoother flow with diminished vorticity effects. Likewise, the axial velocity contours near the casing reveal a significant reduction in low-momentum zones. The increase in static pressure ratio

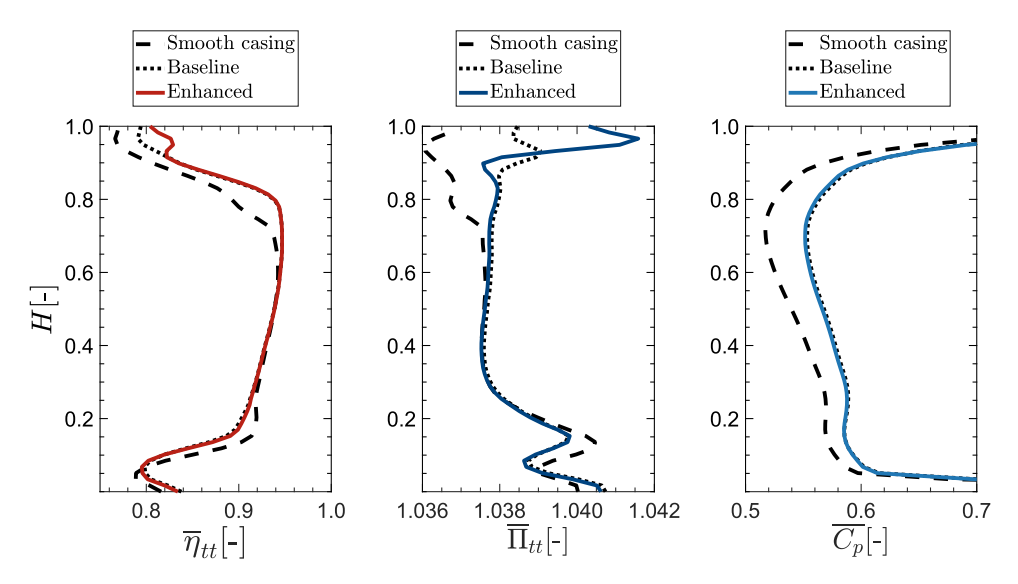


Figure 15. Comparison of span profiles between smooth, baseline, and enhanced configurations. Left: Stage efficiency, middle: Stage total pressure ratio, right: Static pressure rise for the stator.

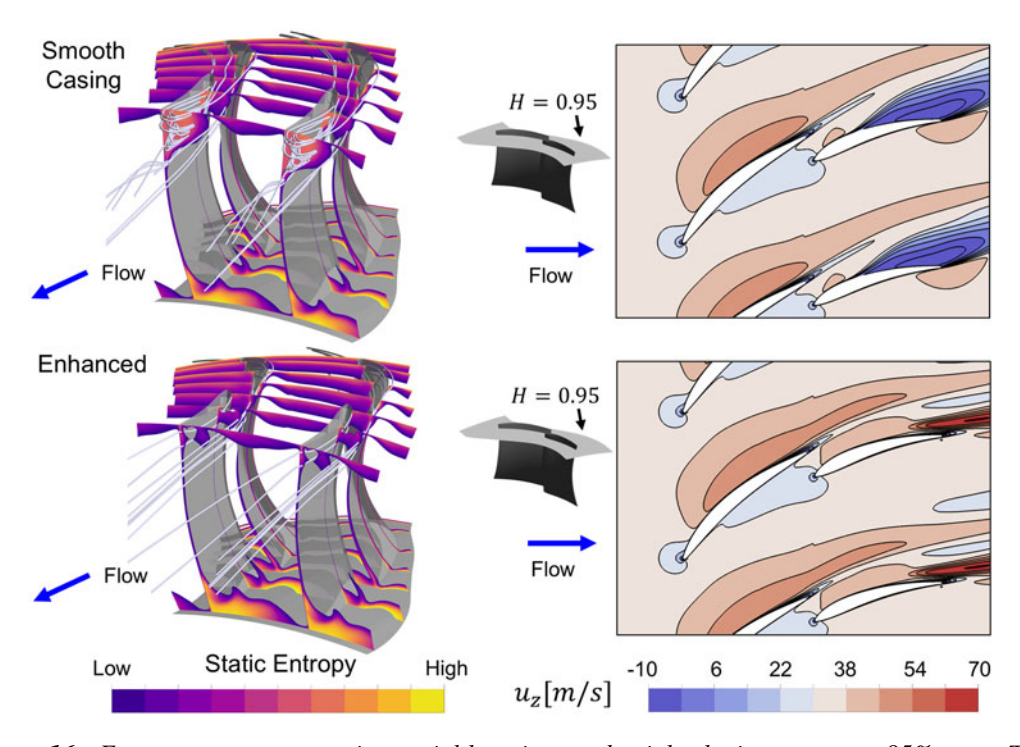


Figure 16. Entropy contours at various axial locations and axial velocity contour at 95% span. Top: Smooth casing case, Bottom: Enhanced configuration.

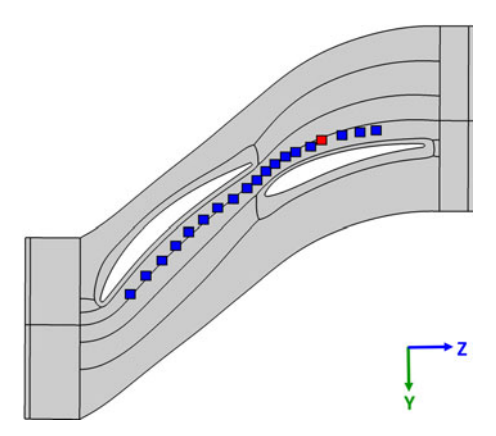


Figure 17. Final injection locations under study. The baseline location is highlighted in red.

also induces slightly more recirculating mass flow in the shrouded cavity, leading to increased blockage, as indicated by the entropy distribution near the hub.

5.5 Effects of injector location

This section examines how the location of the injector affects the aerodynamic performance of the compressor. The analysis focuses on the region along the pressure side of the front vane and the suction side of the rear vane. Areas on the suction side of the front vane and the pressure side of the rear vane were found to either not improve or negatively impact performance and are therefore not included in this study. Each location was tested using the same enhanced configuration selected in the previous section and maintained the same relative injection mass flow rate $\dot{m}_{inj}/\dot{m}_{stall}$. The only variable that changed with the location was the jet angle β , with multiple simulations conducted at each location to identify the optimal angle. In this context, 'enhanced configuration' refers to a fixed injector geometry ($w_c = 10$ mm, $R_c = 12.5$ mm, $\alpha = 5^{\circ}$) and injection rate ($\dot{m}_{inj}/\dot{m}_{stall} = 0.75\%$), while β is treated as a location-dependent tuning parameter to ensure the jet is directed towards the local separation zone. Additionally, the same level of mesh refinement for the interface between the injector outlet and stator casing, and the same convergence criteria (as presented in Section 4), were applied across all simulations to ensure consistent results. The final analysed locations are shown in Fig. 17, with the baseline location used in the parametric study highlighted in red.

The results of the study of injector locations are detailed in Fig. 18. The efficiency η_u showed greater variability, with a CoV of 24.68%. The maximum increase in η_u is observed at an axial location of 1.2 (20% chord of the rear vane), with an efficiency increment of 0.462%. The analysis indicates that performance improvements are attainable in the transition area between the front and rear vanes, especially within the rear vane region. For η_u increments, the optimal range is found to be between ζ values of 1 to 1.4; beyond this, efficiency starts to drop. The total pressure ratio (Π_u) follows a trend very similar to that of η_u . However, it shows lower sensitivity to changes in injector location with a CoV of 10.86%, as previously found with other studied injection parameters.

The trend of final jet angles, illustrated by the colormap in Fig. 18, shows that the effective β range depends strongly on the axial location of the injector. Injections from the FV pressure side require negative β to steer the jet towards the RV suction side, thereby improving incidence at the rear-vane leading edge and mitigating the endwall separation. In contrast, injections from RV suction-side positions demand positive β , since these sites are already close to the loss region and benefit from directing momentum into the corner deficit. The magnitude of the required jet angle scales with proximity: locations further upstream need larger angles, whereas slots closer to the separation onset require only small

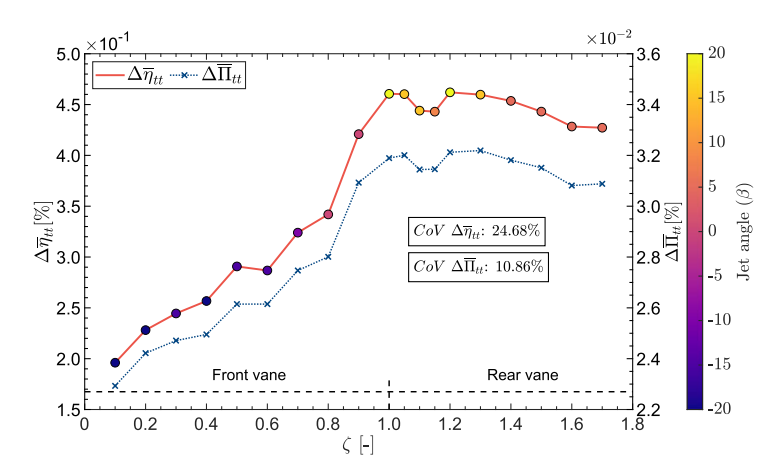


Figure 18. Efficiency and total pressure ratio variations with injector location. The colormap indicates the jet angle (β) , *highlighting regions of maximum aerodynamic benefit between the front and rear vanes.*

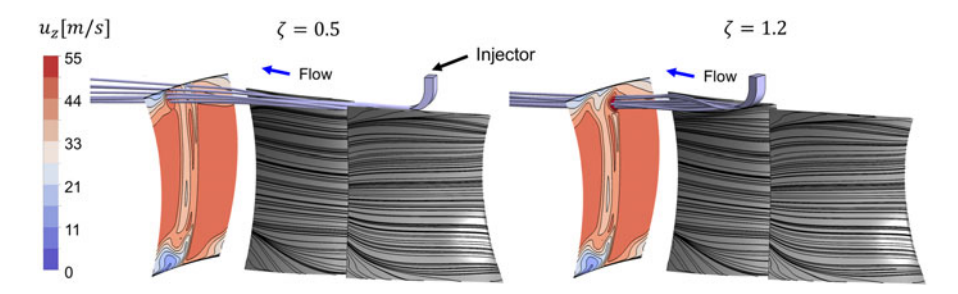


Figure 19. Surface wall and 3D injector velocity streamlines, alongside the axial velocity contour at the stator outlet for two cases of ζ . The jet angle β changes accordingly to the axial location of the injector.

adjustments. For example, angles of about 20° are effective at $\zeta=1.2$, while values near 5° suffice further downstream. These results confirm the jet-angle sensitivity guideline, showing that performance is maintained across a moderate range of β values as long as the jet targets the separation zone, with β naturally adapting to injector placement rather than being fixed to a single value.

Building on this trend, Fig. 19 compares the effect of the selected jet angles across two representative injection positions at $\zeta=0.5$ and $\zeta=1.2$. For $\zeta=0.5$, the best performance is obtained by directing the flow towards the leading edge of the rear vane; however, because the injection is located far upstream of the separation onset, the jet diffuses and loses most of its momentum before reaching the critical region. In contrast, at $\zeta=1.2$, which lies just upstream of the separation point, the boundary layer is more effectively removed. Such conclusions, previously reported for configurations with single aerofoils [36], are here extended to tandem vanes, providing the first evidence of these effects in published literature.

For the subsequent analysis, distinctive cases identified in the study of injection locations are selected. Specifically, two front vane locations at $\zeta=0.1$ and $\zeta=0.5$ are chosen to illustrate lower and mid-range performance, respectively. In contrast, rear vane locations at $\zeta=1.05$ (near the leading edge) and $\zeta=1.2$ are selected for their notable impacts on η_{tt} and Π_{tt} . Further locations at $\zeta=1.4$ and $\zeta=1.6$ are included to characterise behaviour at and beyond the separation point. These selections are detailed in Table 6 and will be used for a detailed analysis of span profiles.

Figures 20 and 21 showcase the span profiles for η_{tt} and Π_{tt} for selected injection location cases, highlighting divergent behaviours above 85% span. The impact of injection becomes evident beyond

Case Label	Description
Front $\zeta = 0.1$	Least optimal case at the design point
Front $\zeta = 0.5$	Mid-range performance case
Rear $\zeta = 1.05$	Near maximum $\Delta \bar{\eta}_{tt}$, at the leading edge
Rear $\zeta = 1.2$	Maximum efficiency increment case
Rear $\zeta = 1.4$	At the separation point
Rear $\zeta = 1.6$	After separation point

Table 6. Selected injection location cases for detailed analysis

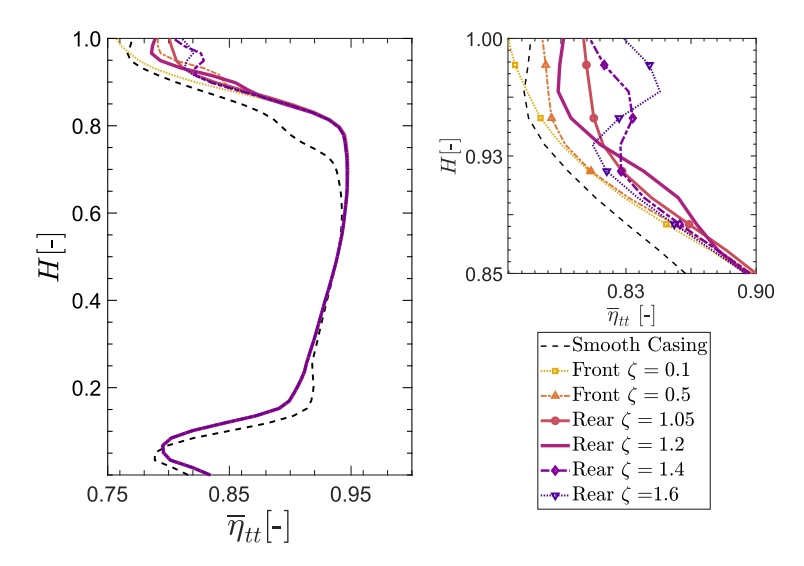


Figure 20. Spanwise distributions of polytropic efficiency for highlighted injection cases. A zoomed-in view shows behaviour between H = 0.85 and 1.0.

60% span, with all cases showing increased values compared to the smooth casing scenario. For efficiency, cases near the rear vane leading edge ($\zeta=1.05$ and $\zeta=1.2$) exhibit a uniform and significant increase across a wider span, suggesting enhanced mixing. Specifically, $\zeta=1.05$ exhibits a consistently smoother efficiency rise, whereas $\zeta=1.2$ shows superior performance at lower span values, diminishing towards H=1.0. For the total pressure ratio, the rear-injection cases show localised differences confined to the near-casing region, with Π_{tt} peaking close to H=1.0. In particular, $\zeta=1.2$ exhibits a distinct peak around H=0.9, indicating concentrated injected flow at this location. This profile behaviour aligns with the jet angle β for this case, set at 20° , since larger β values direct the jet more strongly toward the blade surface and shift the high-energy flow towards lower span zones. These variations are highlighted by the zoomed x-axis in Fig. 21 but become less pronounced once mass-flow averaging is applied, as seen later in the speedline results.

Overall, for larger ζ values beyond the separation point, the influence of injection is confined to a smaller span region due to diminished mixing. Near the hub, at H = 0.4, flow redistribution minimally affects dynamics around the shrouded cavity for all cases.

5.6 Effect of injection on tandem stator loading

In this section, the impact of air injection on blade loading is analysed at the design point condition. Figure 22 compares the smooth casing and a representative injection case at $\zeta = 1.2$, both evaluated at H = 0.9. The blade loading profiles of Ma_{is} are plotted against the normalised chordwise location s, and

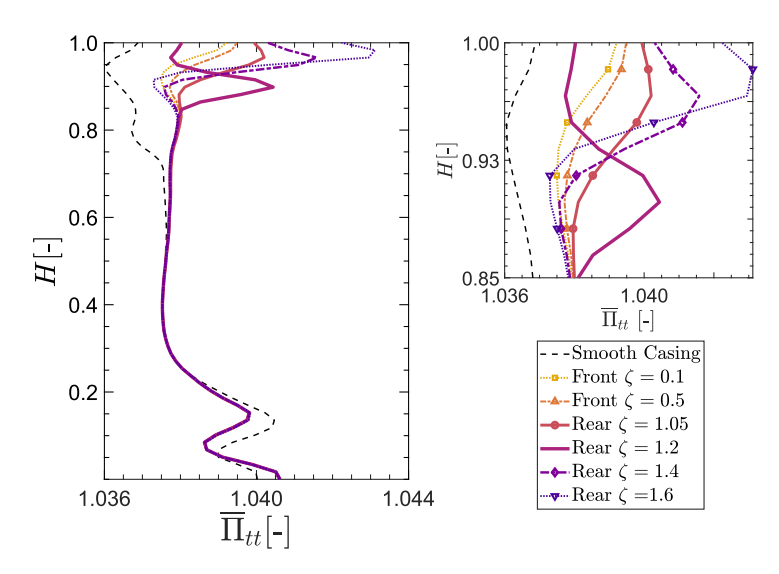


Figure 21. Spanwise distributions of total pressure ratio for highlighted injection cases. A zoomed-in view shows behaviour between H = 0.85 and 1.0.

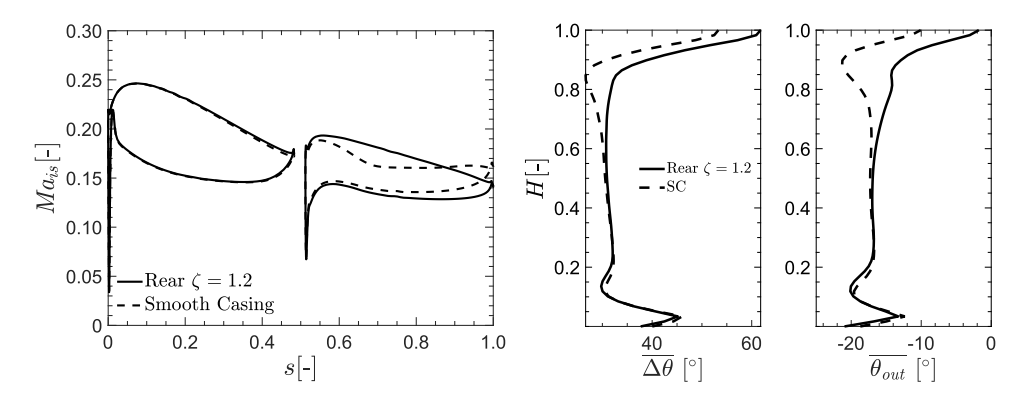


Figure 22. Injection impact on aerodynamic loading. Left: Blade loading profiles at H = 0.9 comparing the smooth casing and an injection case with $\zeta = 1.2$, showing the isentropic Mach number. Right: Turning $\Delta\theta$ and outlet flow angle θ_{out} profiles at the stator outlet for both cases.

additional aerodynamic parameters such as turning $\Delta\theta$ and the flow angle at the stator outlet θ_{out} are presented. As observed in the Ma_{is} curves, the induced loading due to injection is evident in the rear vane compared to the smooth casing case, showing the removal of corner separation near the casing. This removal of low-momentum flow unlocks additional diffusion capacity in the rear vane.

The overall mass-flow averaged diffusion factor DF for the injection case is 0.54, compared with 0.521 for the smooth casing. The increase is entirely attributable to the rear vane, with an independent value of 0.29 for injection versus 0.27 for the smooth casing. Consequently, the turning $\Delta\theta$ of the stator row increases, and the outlet flow angle θ_{out} shows higher values for H>0.6, indicative of the enhanced rear vane loading. Correcting underturning with air injection not only improves blade loading and stage efficiency but also benefits the incidence for subsequent stages and, therefore, overall efficiency in multistage compressors.

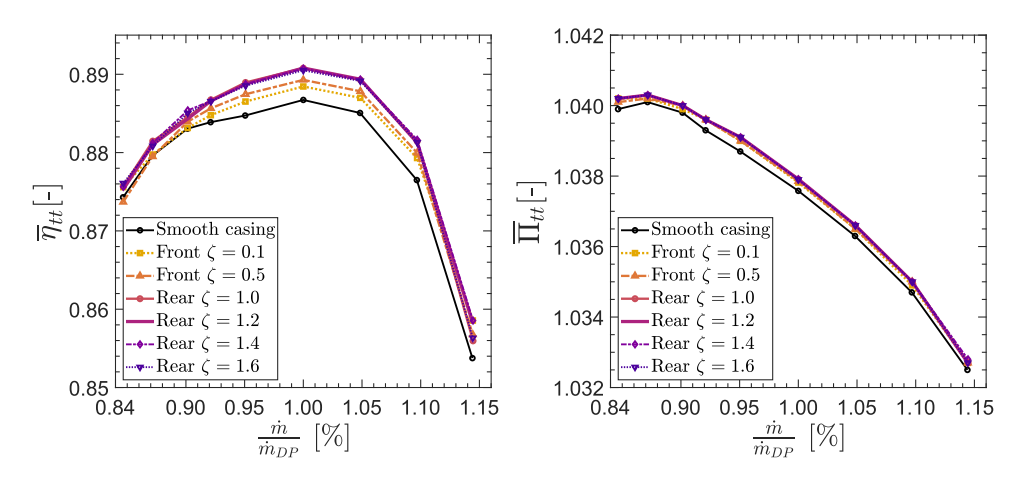


Figure 23. Comparative impact of injection location on stage polytropic efficiency (left) and total pressure ratio (right) under various operating conditions.

5.7 Impact at off-design conditions

We present the impact of the selected configurations under off-design conditions. The relative injection mass flow rate, $\dot{m}_{inj}/\dot{m}_{stall}$, is kept constant, which leads to variations in the total pressure of the injected fluid across different operating points, from de-throttled to near-surge conditions. This variation correlates with an increase in static pressure at the injection site, typically seen when the injector is fed by downstream flow. The simulations start at the design point and systematically progress towards de-throttled and surge conditions by adjusting the outlet mass flow rate. As a reminder, the speedlines presented in this section were obtained using the 'equal inlet mass flow' method described in Section 4, imposing the outlet mass flow rate but setting its value so that the resulting inlet mass flow matches the smooth-casing case. In this way, direct comparability between the smooth-casing and injection cases is ensured at each operating point.

For all injection cases, stage efficiency η_{tt} exceeds that of the smooth-casing scenario in Fig. 23. Notably, the cases near the rear vane consistently outperform those at the front vane across the speedline. The incremental benefit follows a clear trend: it decreases towards throttled/near-surge conditions and increases towards de-throttled conditions. For example, the increment of the enhanced case ($\zeta = 1.4$) at $\dot{m}/\dot{m}_{DP} \approx 1.10$ is about +0.78%, larger than the +0.43% observed at the design point. This behaviour is consistent with the mechanism: at higher mass flow, negative incidence on the front vane strengthens the endwall deficit convected into the tandem gap, enlarging the suction-side separation of the rear vane in the smooth-casing baseline. Injection mitigates this effect, recovering a greater fraction of the loss. Beyond the de-throttled regime, the profiles gradually converge and approach the smooth-casing curve.

Conversely, the total pressure ratio differences between locations are minimal, with all injection cases outperforming the smooth-casing scenario. It is also important to note that while injection in the tandem stator does not extend the stall range-predominantly determined by rotor tip flow—it enhances stage performance across the entire operating range.

5.8 Sensitivity to turbulence model

The baseline simulations in this study were performed with the SST turbulence model, consistent with prior FRANCC numerical setups. While SST is standard in compressor CFD, it is known to have limitations in predicting streamline curvature effects and reattachment in separated flows. Nevertheless, SST has been shown to reproduce tandem-stator separation patterns in related low-speed compressor experiments [11], so it provides a reasonable baseline. To assess the robustness of our findings, two alternative

configuration retailive to the SC			
Turbulence Model	$\Delta\eta_{\scriptscriptstyle tt} [\%]$	$\Delta\Pi_{tt}$ [%]	
SST (baseline)	0.43	0.047	
SST+RM	0.127	0.041	
SST+ γ -Re $_{\theta}$	0.127	0.042	

Table 7. Design-point increments of the enhanced configuration relative to the SC

models were also tested: SST with the reattachment modification (SST+RM) and SST with the γ -Re $_{\theta}$ transition model [26]. These comparisons were restricted to a single representative case—the enhanced configuration—at the design point and, where feasible, along the speedline.

For consistency, the same turbulence intensity of 5% was applied at the injector inlet as in the baseline setup. Since the turbulence level of the jet could in principle influence reattachment by enhancing local mixing, injector turbulence intensity was additionally varied between 1%, 5% and 10% for the enhanced configuration. The resulting increments in total pressure ratio were identical within solver output precision, while the changes in efficiency were negligible: the coefficient of variation across the cases was below 10^{-4} for all models, much smaller than the reported performance increments (0.1-0.6%). This confirms that the dominant factor for reattachment is the injected momentum flux rather than the prescribed turbulence intensity.

A quantitative design-point summary is given in Table 7, reporting the increments of the enhanced configuration relative to the SC for the three models. As seen in Table 7, the alternative models predict similar increments in total pressure ratio, while the efficiency gain is reduced compared with the baseline SST. Since the γ -Re $_{\theta}$ model produced design-point results nearly identical to the reattachment modification but encountered convergence difficulties at off-design operating points, its results are included in the table for comparison only. Although the mesh resolution was sufficient, these convergence issues are not unexpected, as the transition model introduces additional transport equations and can be sensitive in strongly three-dimensional separated flows. At the design point, the γ -Re $_{\theta}$ result indicated $\gamma \approx 1$ throughout the passages, confirming fully turbulent boundary layers. Local values of $\gamma \approx 0.02$ were present in the wall-adjacent cells as part of the near-wall treatment described in the ANSYS CFX-Solver Modelling Guide⁽²⁶⁾. The detailed flow-field comparison below focuses on SST vs. SST with reattachment modification.

Figure 24 compares the baseline SST (top row) and SST with the reattachment modification (bottom row). For each model, the left block shows the SC and the right block the enhanced configuration. Within each block, the left subpanel plots axial-velocity contours on the spanwise plane $H \approx 0.95$, whereas the right subpanel shows the suction-side skin-friction coefficient C_f with limiting streamlines over the full surface; the dashed line on the C_f plots marks where the $H \approx 0.95$ plane intersects the blade. For the smooth casing, SST predicts a larger suction-side separation bubble, a broader low C_f region, and stronger streamline divergence; SST+RM yields a shorter separated region with earlier reattachment. With the enhanced injector, both models produce very similar patterns: the suction side exhibits higher C_f , the limiting streamlines remain attached, and the corner region is stabilised. This confirms that the injection mechanism remains effective regardless of the turbulence model.

The differences in predicted increments are consistent with each model's eddy-viscosity behaviour under adverse pressure gradients. Plain SST generates relatively high turbulent viscosity in the separated shear layer, which diffuses momentum gradients and tends to exaggerate the extent of separation. The reattachment modification reduces this overproduction, yielding thinner shear layers and stronger natural entrainment of high-momentum fluid into the bubble, and thereby smaller pockets. While this explains the lower absolute gains in η , the central conclusion remains unchanged: in all models, injection acts as an artificial entrainment mechanism that robustly suppresses the suction-side separation. In the absence of experimental reference for this preliminary geometry, these results are best interpreted as a robustness assessment of the modeling approach.

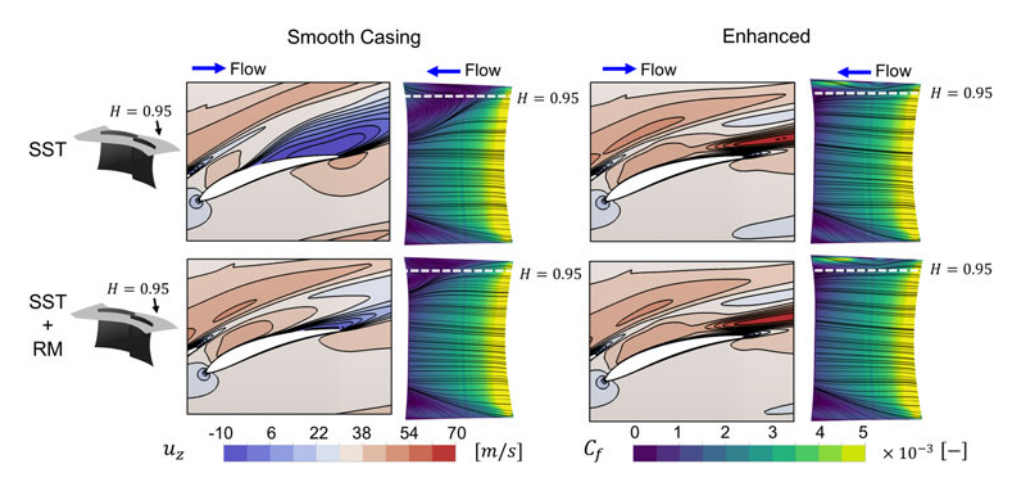


Figure 24. Rear vane flow for SST (top) and SST+RM (bottom). Each block shows axial velocity contours on $H \approx 0.95$ span plane and suction-side C_f with limiting streamlines for the smooth casing and enhanced configurations. Flow direction is indicated by arrows.

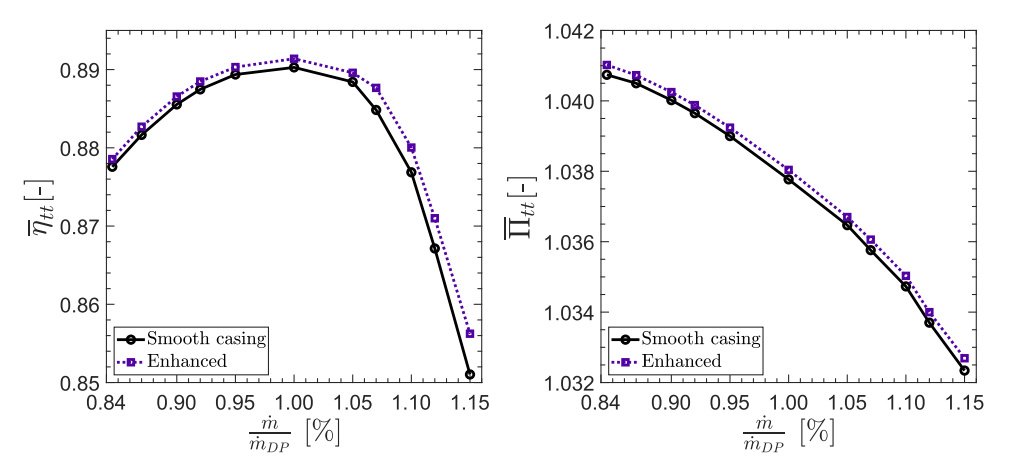


Figure 25. Speedlines for SST with reattachment modification: comparison of SC and enhanced configuration.

To extend the comparison beyond the design point, Fig. 25 shows speedlines for the reattachment-modified SST model. The trends are consistent with those seen for the baseline SST: the enhanced configuration outperforms the smooth casing across the entire operating range, although the absolute increments vary. At the design point the efficiency gain is about +0.13%, but toward de-throttled conditions the improvement increases, reaching +0.36% at $\dot{m}/\dot{m}_{DP}=1.1$ and +0.61% at 1.15. This reflects the flow physics at these conditions, where negative incidences amplify suction-side separation of the rear vane as already discussed in Section 5.7. In contrast, increments diminish toward throttled conditions, where smooth-casing and injection cases converge. For the total pressure ratio, the behaviour follows the same trend but with smaller relative differences. Overall, while the absolute magnitudes of η_{tt} and Π_{tt} vary with the turbulence model, the reduction of suction-side separation and the associated performance gains are consistently predicted, confirming that injection provides a robust means of mitigating endwall-driven corner separation, with the strongest benefit under conditions where separation is most severe.

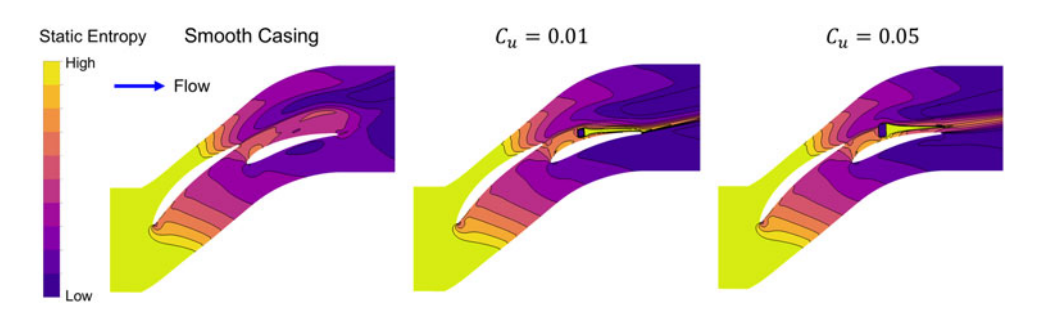


Figure 26. Comparison of the effects on static entropy at the stator casing for the smooth casing case and different injection strategies: small ($C_u = 0.01$) and larger ($C_u = 0.05$) momentum coefficients.

5.9 Injection losses

Throughout this study, our goal was to analyse the aerodynamic impact of injection in a tandem stator configuration and understand how an injection strategy characterised by the momentum coefficient C_u correlates with improvements in stage efficiency and total pressure ratio. Therefore, the source of the injected mass and the potential penalties incurred were not subjects of study. However, in realistic operational conditions, the injection implementation can provoke additional losses in the system.

One common approach to account for total losses, including those from injection, is presented in the work of Evans et al. [32]. According to this study, the total pressure loss coefficient, denoted as ω_t , is defined by a mass-weighted approach that accounts for both the main flow and injected jet contributions. The total pressure loss coefficient is given by:

$$\omega_{t} = \frac{\dot{m}_{in} \left(\overline{P_{t,in}} - \overline{P_{t,out}} \right) + \dot{m}_{inj} \left(\overline{P_{t,inj}} - \overline{P_{t,out}} \right)}{\dot{m}_{in} \left(\overline{P_{t,in}} - \overline{P_{in}} \right) + \dot{m}_{inj} \left(\overline{P_{t,inj}} - \overline{P_{inj}} \right)}$$
(5)

where \dot{m}_{in} and \dot{m}_{inj} denote the mass flow rates of the main and injected streams; $\overline{P}_{t,in}$ and $\overline{P}_{t,out}$ are the mass-flow-averaged total pressures at the tandem stator inlet and outlet, as shown in Fig. 3; and $\overline{P}_{t,inj}$ is the mass-flow-averaged total pressure at the injector inlet. This relationship takes into account the total pressure losses with respect to the total kinetic energy in the tandem stator domain. When \dot{m}_{inj} is equal to zero, we obtain the standard definition of the total pressure loss coefficient ω .

Taking Equation (5) into consideration, we present an example illustrating an injection strategy that accounts for injection losses. As before, the normalised axial location is set at $\zeta=1.4$. However, this time a circumferential width w_c of 6 mm and an injection rate ratio $\dot{m}_{inj}/\dot{m}_{stall}$ of 0.25% are chosen to minimise the generated losses. This configuration results in a momentum coefficient C_u of 0.01 and a ratio u_{inj}/u_{∞} of 1.2, in contrast to the enhanced configuration presented in Section 5.4, which had $C_u=0.05$ and $u_{inj}/u_{\infty}=2.1$.

As shown previously in Fig. 16, the reduction of entropy along the axial direction after the injection location indicates effective mixing of the injected flow with the main flow. However, the entropy contours at the stator casing, shown in Fig. 26, reveal an increase in entropy due to the injection itself. This requires consideration of additional losses using Equation (5). For the larger momentum coefficient case ($C_u = 0.05$), the total pressure loss coefficient ω_t is 0.0494, which is slightly higher than in the smooth casing case. In contrast, for the smaller momentum coefficient case ($C_u = 0.01$), the calculated total pressure loss coefficient ω_t is 0.04396, compared to 0.04350 when injection effects are not considered, indicating that the injection-induced losses are negligible. Despite this, the calculated ω_t still represents a reduction of 5.1% compared to the smooth casing case, where ω is approximately 0.0462. Additionally, an increase in polytropic efficiency η_{tt} of about 0.28% is observed.

Figure 27 shows the comparison of this injection configuration ($C_u = 0.01$) with the smooth casing case and the equivalent higher momentum coefficient configuration ($C_u = 0.05$). A lower momentum coefficient configuration yields a lower increment but still offers aerodynamic improvements. As seen

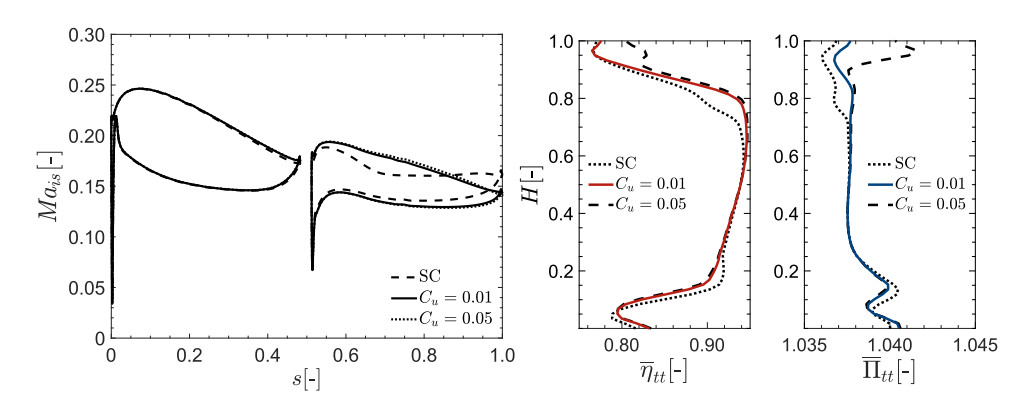


Figure 27. Comparison of injection strategies with small ($C_u = 0.01$) versus larger ($C_u = 0.05$) momentum coefficients to minimise injection losses, for cases at $\zeta = 1.4$. Left: Blade loading profiles at H = 0.9 showing the isentropic Mach number. Right: Polytropic efficiency and total pressure ratio profiles.

in the efficiency and total pressure ratio profiles, the main difference is the behaviour at span values H > 0.9, very close to the casing, where the higher momentum jet shows a pronounced influence. However, the effect of unlocking more diffusion in the rear vane of the tandem stator remains with smaller injection rates, as observed in the blade loading profiles. This approach presents a conservative method to account for injection losses. However, further adjustments may be necessary for each specific application. For instance, utilising a recirculation channel to extract air from the endwall region of the second-stage rotor and re-inject it into the tandem stator in the first stage could enhance performance in other critical areas of the compressor, such as mitigating rotor tip leakage. This highlights the importance of an integrated approach to flow control evaluation, rather than relying on isolated assessments.

6.0 Conclusions

The implementation of air injection was numerically studied in a tandem stator shroud of a low-speed axial compressor, with the primary goal of enhancing compressor performance. The analysis of the smooth-casing case identified flow separation issues in the stator flow, producing significant aerodynamic losses, leading to efficiency drops and suggesting the potential application of air injection to mitigate these effects. As a starting point, an injector baseline configuration was selected, and subsequently, a detailed parametric study was conducted to examine the influence of the injector geometry. The relationship between circumferential width (w_c) and relative injection mass flow rate $\dot{m}_{inj}/\dot{m}_{stall}$ emphasised the need for a careful balance between injection velocity and momentum to achieve aerodynamic improvements without adversely affecting flow stability. This interaction was consistently captured through the momentum coefficient C_u and the velocity ratio u_{inj}/u_{∞} , which directly correlated with improvements in efficiency and total pressure ratio. The final enhanced configuration featured a circumferential width w_c of 10 mm and an injection mass flow rate ratio $\dot{m}_{inj}/\dot{m}_{stall}$ of 0.75%, showing performance enhancements, achieving a 0.43% increase in polytropic efficiency η_u and a 0.047% increase in total pressure ratio Π_u over the smooth-casing scenario.

The study of injector placement identified the most effective locations within the transition area between the front and rear vanes, particularly on the suction side of the rear vane at ζ values of 1.0–1.4. The largest increment in efficiency, 0.462%, was observed for $\zeta = 1.2$, just upstream of the separation point, confirming similar conclusions previously reported for single-aerofoil configurations. The example case with injection at $\zeta = 1.2$ showed blade loading enhancement in the rear vane, evident from the increased diffusion factor and stator turning, effectively mitigating corner separation and improving flow dynamics at the design point. Under off-design conditions, the analysis indicated that injector

locations near the rear vane improved stage efficiency across the full operating range. The incremental benefit was most pronounced towards the de-throttled side of the speedline, reaching about +0.78% at $\dot{m}/\dot{m}_{DP} \approx 1.10$, while diminishing towards throttled conditions. At the same time, the injection strategy did not extend the stall margin, which remains governed by rotor tip flow characteristics.

The robustness of these findings was also tested against different turbulence models. Comparisons of SST, SST with reattachment modification, and SST with the γ -Re $_{\theta}$ transition model showed that while the predicted magnitude of efficiency gain varied, the suppression of suction-side separation and the associated performance improvement were consistently reproduced. Likewise, variations in prescribed injector turbulence intensity had a negligible impact on performance. This confirms that the observed injection mechanisms are governed primarily by momentum flux and remain robust with respect to turbulence modeling choices.

Taken together, the sensitivity studies across geometry, injector placement, operating conditions, and turbulence models reveal consistent trends that can serve as design guidelines. Injection is most effective when applied close to the onset of rear-vane suction-side separation; the jet angle β should be oriented towards the corner deficit while avoiding extreme deflections; the inclination angle α kept relatively small to ensure a tangential introduction; and the radius of curvature R_c chosen sufficiently large to promote Coandă attachment without exceeding realistic exit velocities. The circumferential width w_c and injection mass flow rate $\dot{m}_{inj}/\dot{m}_{stall}$ act in combination and are best interpreted through the momentum coefficient C_u and the velocity ratio u_{inj}/u_{∞} . These guidelines proved robust across operating points and turbulence models, suggesting that the underlying trends extend beyond the specific compressor configuration studied here. Future work could apply these guidelines within a dedicated injector design process, for example by combining them with optimisation methods or experimental assessments. Such studies could vary multiple parameters simultaneously to refine the final geometry and placement, building on the present results to deliver a practical injection concept for implementation.

While the scope of the study was to analyse the aerodynamic effects of air injection strategies in a tandem stator configuration, it is essential to acknowledge that implementing such strategies in real-world scenarios may introduce additional losses. Through a specific example incorporating total losses, our study demonstrated that a positive injection strategy remains viable, with lower mass flow rates or momentum coefficients helping to keep additional losses to a minimum. Translating such strategies into practical compressor applications will require refined studies to establish realistic injection and bleed mass flow rates and their impact on system-level performance. This finding emphasises the potential of air injection as a beneficial aerodynamic strategy in tandem stator configurations, provided that it is implemented with precision and a comprehensive understanding of its impact on overall system efficiency.

Acknowledgments. This research was conducted as part of the AKTIVER project, funded by the German Aerospace Centre (DLR) under the LUFO VI-2 programme.

References

- [1] Dinh, C.-T. and Kim, K.-Y. Effects of air injection on aerodynamic performance of a single-stage transonic axial compressor, *Des. Construct. Maintenan. Open Access Int. J. Eng.*, 2021, 1, pp 24–32.
- [2] Dinh, C.-T., Ma, S.-B. and Kim, K.-Y. Aerodynamic optimization of a single-stage axial compressor with stator shroud air injection, AIAA J., August 2017, 55, (8), pp 2739–2754.
- [3] Cao, Z., Gao, X., Zhang, X., Zhang, F. and Liu, B. Influence of endwall air injection with discrete holes on corner separation of a compressor cascade, *J. Therm. Sci.*, 2021, **30**, (5), pp 1684–1704.
- [4] Cao, Z., Song, C., Gao, X., Zhang, X., Zhang, F. and Liu, B. Effects of pulsed endwall air injection on corner separation and vortical flow of a compressor cascade, *Eng. Appl. Comput. Fluid Mech.*, 2022, **16**, (1), pp 879–903.
- [5] Culley, D.E., Bright, M.M., Prahst, P.S. and Strazisar, A.J. Active flow separation control of a stator vane using embedded injection in a multistage compressor experiment, ASME J. Turbomach., January 2004, 126, (1), pp 24–34.
- [6] Wundrow, D.W., Braunscheidel, E.P., Culley, D.E. and Bright, M.M. Separation control in a multistage compressor using impulsive surface injection, NASA Technical Memorandum TM-2006-214361, NASA Glenn Research Center, Cleveland, OH, USA, July 2006.

- [7] Braunscheidel, E., Culley, D. and Zaman, K. Application of synthetic jets to reduce stator flow separation in a low-speed axial compressor, In *Proceedings of the 46th AIAA Aerospace Sciences Meeting and Exhibit*, Reno, NV, USA, January 7–10, 2008. Paper AIAA 2008-602.
- [8] Wang, H., Liu, B. and Zhang, B. Passive control with blade-end slots and whole-span slot in a large camber compressor cascade, *J. Appl. Fluid Mech.*, 2021, **14**, (3), pp 703–714.
- [9] Brent, J.A. and Clemmons, D.R. Single-stage experimental evaluation of tandem-airfoil rotor and stator blading for compressors, Part 8, NASA Contractor Report CR-134713, Pratt & Whitney Aircraft, West Palm Beach, FL. USA, 1974.
- [10] Bammert, K. and Beelte, H. Investigations of an axial flow compressor with tandem cascades, ASME J. Eng. Power, October 1980, 102, (4), pp 971–977.
- [11] Tesch, A., Lange, M., Vogeler, K., Ortmanns, J., Johann, E. and Gümmer, V. An experimental investigation of a tandem stator flow characteristic in a low-speed axial research compressor, In *Proceedings of ASME Turbo Expo 2014: Turbine Technical Conference & Exposition*, Düsseldorf, Germany, June 16–20, 2014, Paper GT2014-26104.
- [12] Foret, J., Franke, D., Klausmann, F., Schneider, A., Schiffer, H.-P., Becker, B. and Müller, H. Experimental aerodynamic and aeroelastic investigation of a highly-loaded 1.5-stage transonic compressor with tandem stator, *Int. J. Turbomach. Propul. Power*, 2021, 6, (3), Article 21.
- [13] Eckel, J. and Gümmer, V. Numerical investigation of compressor tandem aerofoils featuring near-endwall modification, J. Phys. Conf. Ser., May 2021, 1909, (1), Article 012019.
- [14] Zhang, L. and Wang, S. A combination application of tandem blade and endwall boundary layer suction in a highly loaded aspirated compressor outlet vane, *Proc. Inst. Mech. Eng. A J. Power Energy*, 2018, 232, (2), pp 129–143.
- [15] Straccia, M. and Gümmer, V. Numerical investigation of non-axisymmetric end wall contouring effects in a low-speed compressor tandem stator, In *Proceedings of the 14th European Conference on Turbomachinery Fluid Dynamics & Thermodynamics (ETC14)*, Gdańsk, Poland, April 12–16, 2021, Paper ETC2021-480.
- [16] Hopfinger, M. and Gümmer, V. Preliminary design of a three-stage low-speed research compressor using tandem vanes, In *Proceedings of the AIAA Propulsion and Energy Forum*, Indianapolis, IN, USA, August 19–22, 2019, Paper AIAA 2019–3909.
- [17] Eckel, J. Konzeption und numerische Auslegung von Hybridschaufeln für die Anwendung in hoch belasteten Axialverdichtern, PhD Thesis, Technische Universität München, 2025, 284 pp.
- [18] Dickens, T. and Day, I. The design of highly loaded axial compressors, ASME J. Turbomach., July 2011, 133, (3), Article 031007.
- [19] Panitz, T. and Wasan, D.T. Flow attachment to solid surfaces: The Coanda effect, AIChE J., January 1972, 18, (1), pp 51–57.
- [20] Strazisar, A.J., Bright, M.M., Thorp, S., Culley, D.E. and Suder, K.L. Compressor stall control through endwall recirculation, In *Proceedings of ASME Turbo Expo 2004: Power for Land, Sea, and Air*, Vienna, Austria, June 14–17, 2004, Paper GT2004-53452, pp 655–667.
- [21] Clemen, C., Schrapp, H., Gümmer, V., Müller, R., Künzelmann, M. and Vogeler, K. Design of a highly-loaded four-stage low-speed research compressor, In *Proceedings of ASME Turbo Expo 2008: Power for Land, Sea, and Air*, Berlin, Germany, June 9–13, 2008, Paper GT2008-50177, pp 181–191.
- [22] Boos, P., Möckel, H., Henne, J.M. and Seimeler, R. Flow measurement in a multistage large scale low speed axial flow research compressor, In *Proceedings of ASME Turbo Expo 1998: Power for Land, Sea, and Air*, Stockholm, Sweden, June 2–5, 1998, Paper 98-GT-94.
- [23] Heinichen, F., Gümmer, V., Plas, A. and Schiffer, H.-P. Numerical investigation of the influence of non-axisymmetric hub contouring on the performance of a shrouded axial compressor stator, CEAS Aeronaut. J., March 2011, 2, (1), pp 89–98.
- [24] Hopfinger, M. Design and aerodynamic analysis of a multistage low-speed axial compressor using tandem stator vanes, PhD Thesis, Technische Universität München, 2024.
- [25] Bardina, J.E., Huang, P.G. and Coakley, T.J. Turbulence modeling validation, In *Proceedings of the 28th AIAA Fluid Dynamics Conference*, Snowmass Village, CO, USA, June 29–July 2, 1997, Paper AIAA 1997-2121.
- [26] Ansys Inc. Ansys CFX, Release 24.2, Help System: CFX-Solver Theory Guide, Ansys Inc., 2024, Chapter 3.
- [27] NUMECA International, IGG/AutoGrid5 User's Guide, 2013.
- [28] Celik, I.B., Ghia, U., Roache, P.J., Freitas, C.J., Coleman, H.W. and Raad, P.E. Procedure for estimation and reporting of uncertainty due to discretization in CFD applications, ASME J. Fluids Eng., July 2008, 130, (7), Article 078001.
- [29] Baojie, L., Zhang, C., An, G., Du, F. and Yu, X. Using tandem blades to break loading limit of highly loaded axial compressors, *Chin. J. Aeronaut.*, April 2022, **35**, (4), pp 58–68.
- [30] Khaleghi, H., Teixeira, J., Tousi, A. and Boroomand, M. Parametric study of injection angle effects on stability enhancement of transonic axial compressors, J. Propul. Power, September—October 2008, 24, (5), pp 1100–1107.
- [31] Denton, J.D. Loss mechanisms in turbomachines, ASME J. Turbomach., October 1993, 115, (4), pp 621–656.
- [32] Evans, S.W. and Hodson, H.P. The cost of flow control in a compressor, In Proceedings of ASME Turbo Expo 2011: Power for Land, Sea, and Air, Vancouver, Canada, June 6–10, 2011, Paper GT2011-45638.
- [33] Kim, H., Rajesh, G., Setoguchi, T. and Matsuo, S. Optimization study of a Coanda ejector, *J. Therm. Sci.*, 2006, **15**, (4), pp 331–336.
- [34] Sarimurat, M.N. and Dang, T.Q. An analytical model for boundary layer control via steady blowing and its application to NACA-65-410 cascade, *ASME J. Turbomach.*, June 2014, **136**, (6), Article 061011.

30 Gutiérrez Lupinta et al.

- [35] Hopfinger, M. and Gümmer, V. Numerical investigation of stator shroud leakage effects in a 1.5-stage low-speed axial compressor, In *Proceedings of the 14th European Conference on Turbomachinery Fluid Dynamics & Thermodynamics* (ETC14), Gdańsk, Poland, April 12–16, 2021, Paper ETC2021-189.
- [36] Fottner, L. Theoretical and experimental investigations on aerodynamically highly-loaded compressor bladings with boundary layer control, In *Proceedings of the 4th International Symposium on Air Breathing Engines (ISABE)*, Orlando, FL, USA, April 6–11, 1980, Paper ISABE 80–7032.